Feasibility of Shielding Correction for Radiation Detectors in LEO

A Geant4 Analysis of Shielding Effects on the Timepix3 Detector aboard OneWeb's JoeySat

Onno Van de Sype

AE5810: Thesis MSc Aerospace Engineering

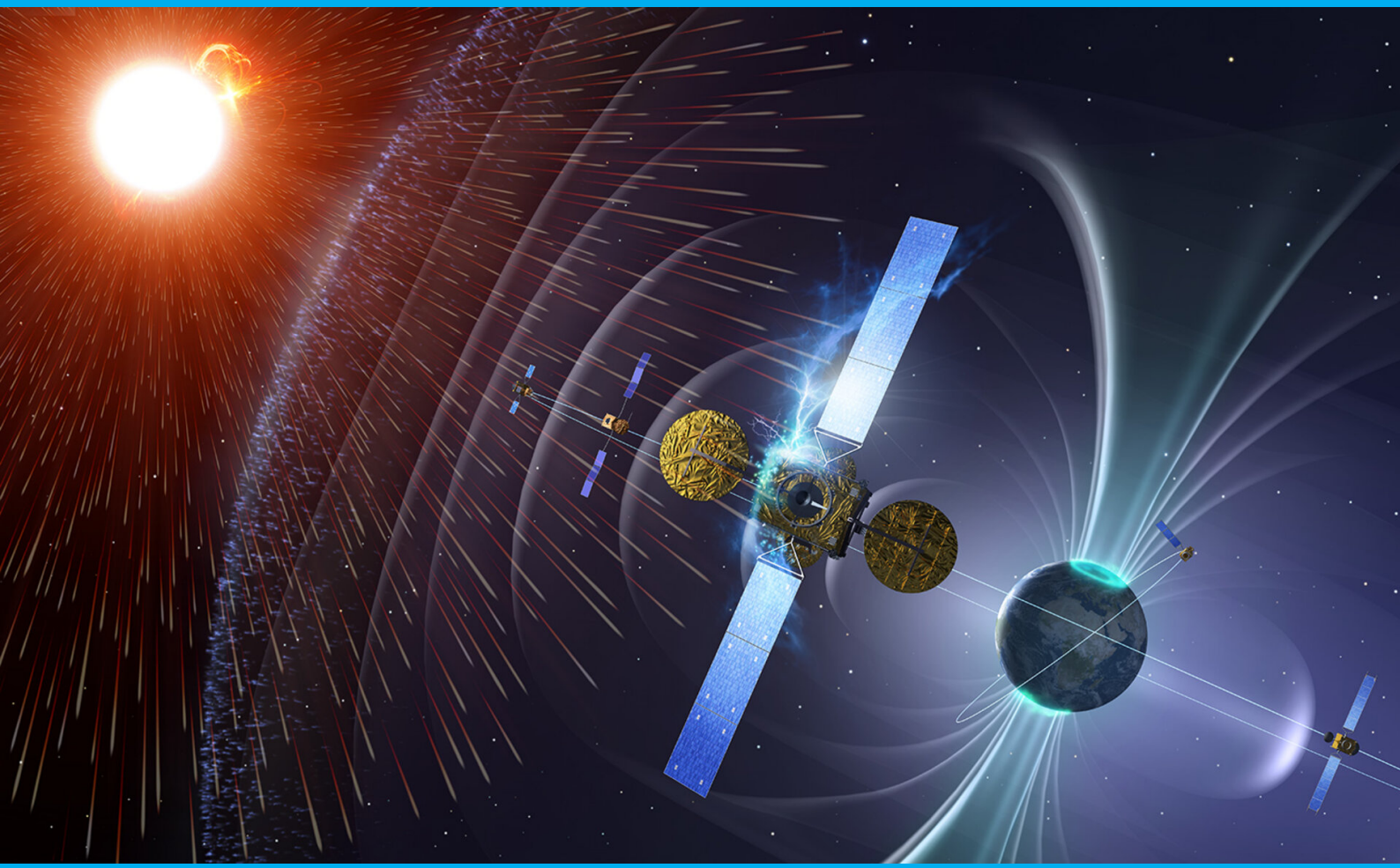

TU Delft

Feasibility of Shielding Correction for Radiation Detectors in LEO

A Geant4 Analysis of Shielding Effects on the Timepix3 Detector aboard OneWeb's JoeySat

by

Onno Van de Sype

Student Name	Student Number
Onno Van de Sype	4850785

Instructor:	Dr C. Granja, Dr A. Menicucci
Institution:	Delft University of Technology
Place:	Faculty of Aerospace Engineering, Delft
Project Duration:	March 2024 - August 2025

Cover Image: *Space radiation affects satellites* - ESA - `https://www.esa.int/ESA_Multimedia/Images/2012/07/Space_radiation_affects_satellites`

TU Delft

Abstract

Measurements of the space radiation environment in Low Earth Orbit (LEO) are critical for satellite safety and operations. However, the inherent shielding of a spacecraft alters the incident radiation field, complicating efforts to reconstruct the true external environment from measurements taken by internal detectors. This thesis investigates the feasibility of developing shielding correction factors for proton radiation measured by a Timepix3 (TPX3) detector.

The research was conducted using the Geant4 Monte Carlo toolkit to model the transport of protons through a $5\,\mathrm{mm}$ aluminium shield. This simulation framework was first validated against data from ground-based proton accelerator experiments. Empirical models for correcting kinetic energy reduction and particle transmission were then successfully derived from the simulation data.

The validation process confirmed the simulation's accuracy for high-energy protons (>$70\,\mathrm{MeV}$) but revealed a systematic overestimation of energy loss at lower energies (<$40\,\mathrm{MeV}$). The investigation into applying the correction factors uncovered a more basic limitation: an inherent ambiguity exists in the relationship between a proton's deposited energy (E_{dep}) and its kinetic energy (E_{kin}), which prevents a reliable, direct conversion from the detector's measurements.

It is therefore concluded that while theoretical correction models can be formulated, their practical application to shielded detector data is impractical due to the main challenge of reconstructing the incident energy of detected particles.

Acknowledgements

I would first like to express my sincere gratitude to my supervisors, Dr. A. Menicucci and doc. Ing. C. Granja. I am thankful for the opportunity to work on this challenging and interesting topic and for the guidance you have provided throughout this process. Your expertise and feedback have been invaluable in shaping this thesis, and I believe I can call myself lucky for the amount of patience you have had and the time you have spent on supporting me.

I would also like to extend my heartfelt thanks to my family and friends for listening to my frustrations, for their unstoppable belief in me, even when I didn't see it myself, for their patience, and their encouragement during these past months. This journey would not have been possible without you.

And finally, to my dad, who was always so proud of me. I wish you could have seen this finished project.

Onno Van de Sype
Rotterdam, August 2025

Contents

List of Symbols

Symbol	Definition	Units
A	Atomic Mass Number	[g/mol]
I	Mean Excitation Potential	[eV]
T_{max}	Maximum energy loss in head-on collision	[MeV]
v	Velocity	[m/s]
q	Charge	[C]
z	Charge of particle	[-]
Z	Atomic Number	[-]
dE/dx	Stopping Power/LET	[MeV/cm or keV/μm]
β	Velocity in terms of c	[-]
σ	Nuclear Cross Section	[b]
ρ	Density	[kg/m^3 or g/cm^3]

List of Abbreviations and Acronyms

Acronym	Meaning
ALARA	As Low As Reasonably Achievable
ARS	Acute Radiation Syndrome
CME	Coronal Mass Ejection
DD	Displacement Damage
DSB	Double-Strand Break
ESA	European Space Agency
EVA	Extravehicular Activity
GCR	Galactic Cosmic Ray
LEO	Low Earth Orbit
LET	Linear Energy Transfer
MC	Monte Carlo
NASA	National Aeronautics and Space Administration
ROS	Reactive Oyxgen Species
SAA	South Atlantic Anomaly
SC	Surface Charging
SEB	Single Event Burnout
SEE	Single Event Effect
SEGR	Single Event Gate Rupture
SEL	Single Event Latch-up
SEP	Solar Energetic Particle
SEU	Single Event Upset
SPE	Solar Particle Event
SPE	Solar Proton Event
SSB	Single-Strand Break
TID	Total Ionising Dose

List of Figures

List of Tables

1

Introduction

Satellites operating in Low Earth Orbit (LEO) are constantly exposed to a harsh radiation environment. [35] This radiation poses a significant risk to sensitive electronic components, leading to performance degradation and potential mission failure. The large fraction of spacecraft anomalies due to radiation can be seen in Figure 1.1.

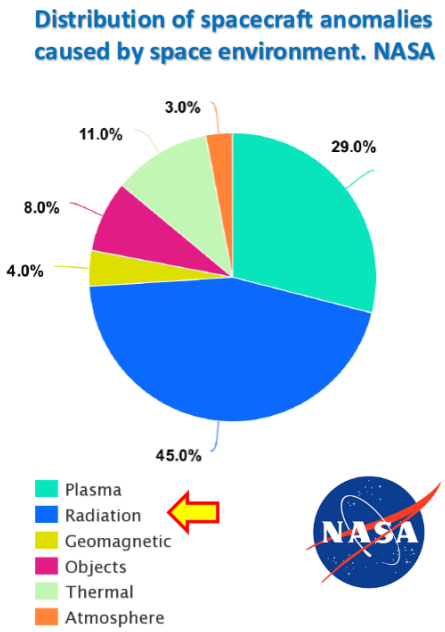

Figure 1.1: Distribution of spacecraft anomalies caused by the space environment. Radiation is the single largest contributor, responsible for 45% of failures. Source: [14]

The space radiation environment is a complex field composed of particles from multiple sources, including trapped particles in planetary magnetospheres, solar events, and galactic cosmic rays, as illustrated in Figure 1.2. Understanding this external field is very important for mission design and safety. However, a significant challenge arises from the fact that measurements are typically conducted from within the spacecraft itself.

While shielding is used to protect these components, it also alters the energy and composition of the radiation field, making it difficult to determine the true external environment from measurements taken inside the spacecraft. The primary objective of this thesis is therefore to investigate the feasibility of developing correction factors to account for these shielding effects, with a focus on the proton radiation measured by the Timepix3 detector aboard OneWeb's JoeySat.

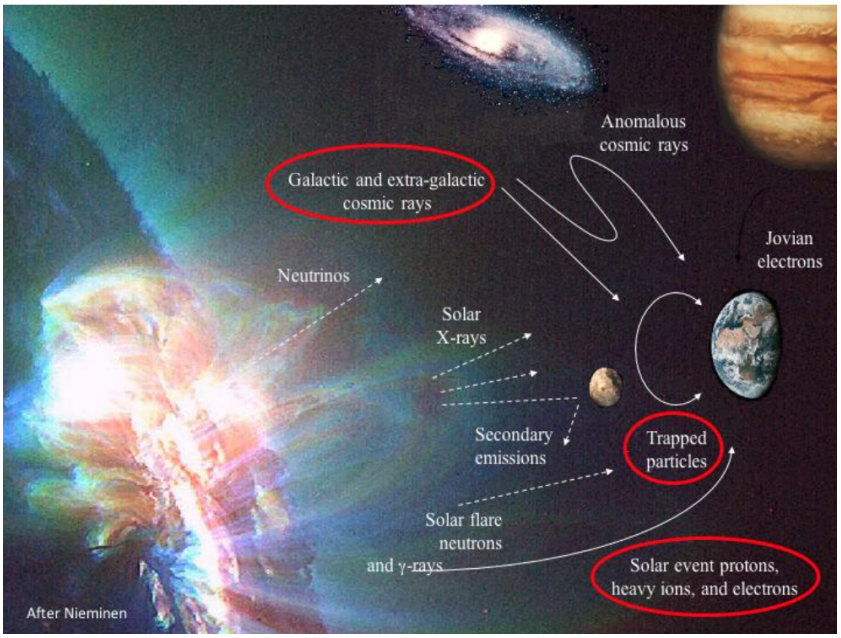

Figure 1.2: An overview of the primary sources of the space radiation environment. Source: [38]

This thesis is structured as follows. Chapter 2 provides a theoretical background on the space radiation environment and the fundamental principles of particle transport through matter. Chapter 3 details the methods and tools used in this research, with a focus on the Geant4 Monte Carlo simulation toolkit. Chapter 4 covers the validation of the simulation model against data from in-beam calibration experiments. Chapter 5 presents the results of the primary simulation of space radiation in a LEO orbit and analyses the shielding effects. Chapter 6 elaborates on the derivation of the shielding correction factors and discusses their application to satellite data. Finally, Chapter 7 presents the overall conclusion of this work and provides recommendations for future research.

2

Radiation Environments, Transport, and Effects of Shielding

This chapter provides the theoretical background necessary to understand the central research problem of this thesis. It begins by defining ionising radiation, its constituent particles, and the physical quantities used to characterise a radiation field. The chapter then explores the fundamental principles of how these particles interact with matter, which leads into a discussion of shielding techniques and their effects. The concepts presented form the basis for interpreting the simulation methodologies and results detailed in the following chapters. Additional background info can be found in Appendix C.

2.1. Ionising Radiation, Types, and Components

Radiation is broadly defined as the emission and transfer of energy through space or matter, in the form of energetic particles or electromagnetic waves.
There are many ways of classifying or describing the various particles and waves that fall under the term radiation. One such way is to divide this according to mass (heavy or light) and charge (charged or neutral). Using this method of classification, an overview can be made as seen in Figure 2.1.

Charged Particles		**Neutral Particles**	
Heavy	**Light**	**Heavy**	**Light**
p	β^-	n	γ
D	Electron		X-ray
T	β^+		ν
α			
Heavy ions without electrons			

Figure 2.1: Classification of Particles according to Kónya et al. (2012) [26]

.

From top to bottom and from left to right, the particles are protons, deuterium, tritium, alpha particles, and heavy ions without electrons for the heavy charged particles. Negative beta particles, electrons, and positive beta particles have a lower mass and are therefore in the light charged group. Neutrons belong in the heavy neutral class and lastly, the γ-rays, X-rays, and the neutrinos. One should note that γ-rays and X-rays are technically not particles but part of the electromagnetic spectrum and can thus be seen as photons [26].

Focus will be on ionising radiation as these have the ability to remove electrons from atoms or molecules, thereby ionising them. This is what causes damage to materials and biological tissue [12, 33]

2.1.1. Characterising the Radiation Field

To describe and measure a radiation field, several physical quantities, or degrees of freedom, are used. The most fundamental of these are the particle's intensity, energy, and direction.

- **Intensity (Flux and Fluence):** In radiation physics, intensity is typically described by **flux**, defined as the number of particles passing through a unit area per unit time (e.g., particles/cm^2/s). When integrated over time, this gives the fluence. The flux is the primary determinant of the radiation dose rate. In the context of shielding, the reduction in intensity is often described as a **transmission percentage**, which is the ratio of the flux measured behind the shield to the incident flux.
- **Energy:** This is a crucial parameter that is often distinguished in two ways: the **kinetic energy** of a particle as it travels through space, and the **deposited energy**, which is the amount of energy a particle loses as it passes through a material, such as a detector sensor. As will be discussed, the relationship between these two energy types is a central challenge of this research.
- **Direction:** This refers to the trajectory of a particle. While the radiation environment in LEO is largely isotropic (arriving from all directions), a particle's angle of incidence significantly impacts its path length through shielding and the detector, which in turn affects the resulting measurement.

2.2. Radiation Interaction with Matter

Radiation interacts with matter in several ways, including interacting with orbital electrons, the nuclear field, or the nucleus itself. During these interactions, radiation particles may transfer some or all of their energy to the material, leading to various results such as absorption or scattering, which can be either elastic or inelastic. These interactions may result in the excitation or ionisation of the material, or in some cases, nuclear reactions or nuclear resonances may occur. The strength of these interactions can vary, ranging from weak to strong depending on the specific conditions [26]. The various possibilities of these interactions of radiation in matter is summarised in Figure 2.2.

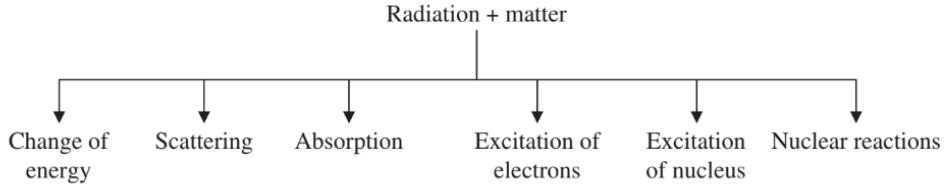

Figure 2.2: Interaction of radiation with matter according to Kónya et al. (2012) [26]

In Figure 2.2, the left three branches relate to the effects on the radiation, while the right three branches depict the changes induced in matter [26]. One should note that another branch can be added to the changes on the matter, namely ionisation. Below, a small overview of all these effects will be given.

- **Change of Energy**: the radiation particle loses energy as it interacts with the material, either through inelastic collisions or other mechanisms.
- **Scattering**: the incident particle changes direction after interacting with the material. This can occur elastically (no energy loss) or inelastically (with energy transfer). In some cases, the particle may produce secondary particles during the interaction.
- **Absorption**: the radiation particle transfers all its energy to the material and ceases to exist as a distinct particle. This process often involves the complete absorption of photons or particles like neutrons.
- **Excitation**: an electron in an atom absorbs part of the radiation's energy and is elevated to a higher energy shell. The electron later drops back to its ground state, releasing energy. Similarly, the nucleus can be excited to a higher energy state and return to its ground state, typically emitting gamma radiation.

- **Nuclear Reaction**: when radiation interacts with the nucleus of an atom, it may alter the nucleus's structure or composition. This can result in processes like fission (splitting of the nucleus), fusion (combining of nuclei), or the formation of a new isotope.
- **Ionisation**: ionisation occurs when a radiation particle transfers enough energy to completely remove an electron from an atom, leaving behind a positively charged ion.

2.3. Shielding Techniques and Effects

In conventional radiation protection, there are three ways of mitigating radiation: 1) increase distance between subject and source; 2) minimise duration of exposure and 3) use shielding between subject and source. In space, the first one is not possible due to the isotropic distribution of space radiation. The second one is only in a limited extend possible, for example by optimising spacecraft trajectories when crossing the radiation belts or reduce the cruise duration in deep space missions. Therefore, shielding is the only option to attenuate the received doses by both spacecraft and astronauts. [39, 12]. In this Section, active and passive shielding will be discussed and their effects on the radiation.

2.3.1. Active & Passive Shielding

This subsection covers two shielding types: active shielding which makes use of actively deflecting the caharged particles, and passive shielding which focuses on stopping, absorbing or attenuating the radiation by adding material between the source and target.

Active Shielding

In his 2001 paper, Townsend provides a foundational overview of active shielding methods to protect spacecraft from space radiation [44]. His study covers four primary methods, each presenting their own challenges, particularly in shielding against GCRs:

- Electrostatic Fields: Townsend determined that electrostatic shields, while capable of deflecting charged particles, are impractical for GCR shielding due to the extreme voltages required, far exceeding the technological limits of that time.
- Plasma Shielding: the plasma shielding concepts involve creating a controlled plasma around the spacecraft using an electrostatic field to repel positively charged particles. Although it looked promising for SEPs, the method faces big challenges for GCR shielding due to plasma instability and high power requirements.
- Confined Magnetic Fields: magnetic fields confined close to the spacecraft have shown some success in SEP shielding but are ineffective against GCRs, with findings suggesting that passive bulk shielding may yield better results with similar mass requirements.
- Unconfined Magnetic Fields: this approach, which involves extending a magnetic field beyond the spacecraft, was primarily developed for space colonies and found to be potentially feasible for SEP shielding. However, the prohibitive mass requirements and complexity make it difficult to implement for GCR protection.

Although Townsend's review was written in 2001, little progress has been made in making these options feasible, largely due to the technical and engineering challenges that remain for these methods [47, 30]. In general, these active shielding concepts remain largely theoretical, and significant advancements in technology are required before practical implementation can be considered for future missions [43].

Passive Shielding

Passive shielding is currently the most practical and effective method to mitigate the effects of space radiation, particularly for long-term missions in interplanetary space [11]. By placing physical materials between the radiation source and the subject, passive shielding reduces the radiation dose through mechanisms like absorption, scattering, and nuclear fragmentation [32]. Unlike other strategies, such as active shielding, which remain technically and energetically challenging as discussed above, passive shielding is well-established and deployable in current spacecraft designs. This section explores the principles of passive shielding, evaluates promising materials, and discusses the challenges of fully

mitigating radiation risks.

Passive shielding works by attenuating incoming radiation through interactions with the material. High-energy particles, such as galactic cosmic rays (GCRs) and solar energetic particles (SEPs), lose energy via electromagnetic interactions, scattering, or breaking into lighter nuclei and neutrons as discussed earlier in this chapter [32]. For example, shielding materials like aluminium or polyethylene attenuate radiation by reducing the energy and altering the fluence of particles passing through them [30]. A visualisation of these interactions can be seen in Figure 2.3

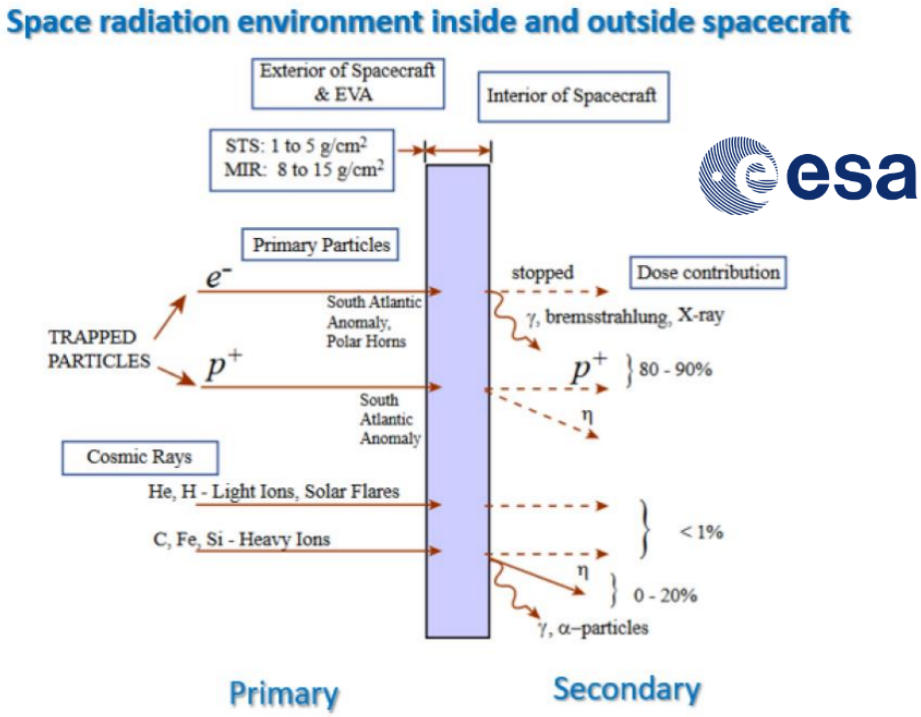

Figure 2.3: A schematic of the space radiation environment inside and outside a spacecraft, illustrating the transformation of primary particles into a secondary radiation field by shielding. Source: [14]

In terrestrial applications, increasing material thickness generally increases shielding effectiveness. However, in the space environment, the high-energy nature of GCRs complicates this relationship. GCR interactions with shielding can produce secondary particles, such as neutrons, which may increase the effective dose [30]. This makes the choice of material crucial to balancing the attenuation of primary particles while minimising secondary radiation, and at the same time, optimising the weight.

Both energy loss and changes in particle fluence are related to the number of atoms per unit mass, which is proportional to Avogadro's number divided by the atomic mass number (A) for each element in the material. The energy loss by ionisation for a single element is proportional to Z/A, where Z is the atomic number, as it determines the number of electrons per atom. However, the energy loss per gram of material (mass stopping power) is inversely proportional to the material density (ρ) [12].

In terms of nuclear interactions, the number of nuclear reactions per unit mass and per unit incident fluence is proportional to σ/A, where σ is the nuclear reaction cross section. To a first approximation, σ scales with $A^{2/3}$, making the nuclear transmission proportional to $1/A^{2/3}$. The ratio of electronic stopping power to nuclear interaction transmission is therefore proportional to (Z/ρ)$A^{2/3}$[12]. This shows that materials with low atomic mass are favoured.

Lightweight materials like hydrogen and carbon are particularly effective, as they have higher Z/A ratios

compared to heavier materials. For instance, Z/A is 1 for hydrogen, 0.5 for carbon, 0.48 for aluminium, 0.46 for iron, and 0.40 for lead. Additionally, the ratio of ionisation energy loss to nuclear interactions depends on the material density. For liquid hydrogen (ρ=0.07g/cm^3), the ratio is approximately 14, whereas for aluminium (ρ=2.7g/cm^3) and lead (ρ=11.3g/cm^3), the ratios are only 0.5 and 0.2, respectively [12].

Historically, shielding addressed only acute risks, with aluminium as the standard material during the Apollo era [3]. Aluminium, still commonly used in spacecraft construction, provides structural support but produces more secondary particles than hydrogen-rich materials [32]. Later, materials like polyethylene (high hydrogen-content) were added, as seen in the ISS, where it reduces radiation doses by approximately 20% in crew sleeping quarters. Water is another promising material, with experimental setups on the ISS showing up to 37% dose reduction using water-soaked towels [10, 30].

Research into advanced materials has identified several promising options for passive shielding. Hydrogen-rich materials, such as polymers reinforced with nano-fillers, are particularly effective due to their high stopping power and reduced secondary radiation production [13]. For instance, polyethylene composites enhanced with carbon nanotubes offer both lightweight properties and efficient shielding [13].

Liquid hydrogen, while highly effective in reducing radiation due to its high energy loss to nuclear interaction ratio, poses challenges in storage and handling [39]. Other materials like water, serve as a versatile shielding material, providing both radiation protection and a potential resource for life support systems in long-term missions [30].

While passive shielding remains the best option for current space missions, it is not without limitations. Shielding is only partially effective against high-energy GCRs, whose long ranges make complete attenuation infeasible. Increasing shield thickness may worsen secondary radiation production, requiring careful material selection to balance protection and weight constraints [30].

Additionally, current knowledge of the stochastic effects of heavy ions in GCRs is insufficient to provide precise risk estimates for long-term missions, underscoring the need for further research into shielding materials and their interactions with high-energy particles, but also for a detailed composition of the radiation fields [39, 12].

2.4. Chapter Summary and Thesis Focus

This chapter has reviewed the principles of the space radiation environment, the nature of particle interactions with matter, and the role of shielding in mitigating radiation effects. It has established that while various strategies exist, passive shielding with common structural materials like aluminium remains the standard for most spacecraft.
With this theoretical background in place, the remainder of this thesis will focus specifically on modelling the effects of a passive aluminium shield on the LEO proton environment. The specific simulation tools and methodologies developed to conduct this investigation are detailed in the following chapter.

3

Methods & Tools

This chapter outlines the methodological framework and tools used to analyse the effect of shielding in the context of the space radiation environment in LEO. In Section 3.1, an overview of the research methodology is given. Afterwards, the experimental data acquisition is discussed in Section 3.2. This then ties into the simulation framework which was set up for this research which is elaborated upon in Section 3.3. Lastly, in Section 3.4, an explanation is given how the data and simulation outputs are processed and which other tools are used in this research.

3.1. Overview of Research Methodology

This study follows a simulation-driven methodology supported by experimental validation and in-orbit satellite data. The research approach began with a literature review to gain a deep understanding of radiation transport through matter and radiation shielding in space environments. Monte Carlo simulations were designed and implemented using Geant4, first to replicate on-Earth mono-energetic beam experiments for validation purposes, and later to model the isotropic space radiation environment. Important steps included the analysis of particle intensity, energy spectra, and secondary particle generation behind shielding which formed the basis for making the correction factors in this thesis. A big challenge, however, is that these correction factors are dependent on a particle's incident kinetic energy. The Timepix3 detector does not measure this value directly. Instead, it measures the deposited energy left by a particle as it passes through the sensor. Therefore, to apply any correction factor to the detector's measurements, a method to first reconstruct the kinetic energy from the measured deposited energy is required. To investigate this step, a backwards propagation model based on the Bethe-Bloch equation was developed and tested on simulated data.

3.2. Experimental Data, Radiation Measurements

In this section, the data acquisition from the Timepix3 detector is discussed. First, in Section 3.2.1, a description of the detector itself will be given. Afterwards, the ground-based experiments are desribed in Section 3.2.2. In Section 3.2.3, a short overview is given of the data collection by the TPX3 detector on board OneWeb's JoeySat.

3.2.1. Timepix3 Detector

The Timepix3 detector is a compact, low-power imaging and particle tracking device with a 256x256 pixel array ($14\,\mathrm{mm}\times14\,\mathrm{mm}$sensitive area). In this case it uses a $500\,\mu\mathrm{m}$ thick silicon sensor material. Other variations exist with various thicknesses of Silicon (Si) or Cadmium Telluride (CdTe). This detector is capable of recording the position, energy, time of arrival, and track shape of individual ionising particles, such as protons, electrons, and X-ray photons. From the track shape, additional parameters like particle type, direction of flight, Linear Energy Transfer (LET), and charge can be determined. The data can be read out instantly in pixel mode at up to 2.3 million hit pixels per second, or accumulated in frame mode and read out at a maximum of 16 frames per second. When an ionising particle interacts with the sensor, it generates an electric charge that is collected by an electric field and amplified in

a pixel preamplifier, forming a voltage pulse. The amplitude and duration of this pulse are directly proportional to the energy deposited by the particle in that pixel. A ”hit” or ”event” occurs when the voltage pulse amplitude in a specific pixel goes over a predetermined threshold. [1]

3.2.2. Ground-Based Experimental Setups

Cyklotron Rez Experiment

In March 2023, well-defined mono-energetic beam experiments were conducted at the Cyklotron Rez facility to calibrate and test the TPX3 detector. The experimental setup involved a proton beam generator producing protons with an energy of $35.5\,\mathrm{MeV}$. The beam had a circular profile with a full width at half maximum (FWHM) of $3\,\mathrm{mm}$. Positioned two metres downstream of the generator along the beam path, a TPX3 detector was used to record the radiation. Between the beam source and the detector, aluminium plates of various thicknesses were inserted at different positions to act as beam degraders. These plates served to reduce the proton energy before reaching the detector. An overview of this experimental arrangement is provided in Figure 3.1.

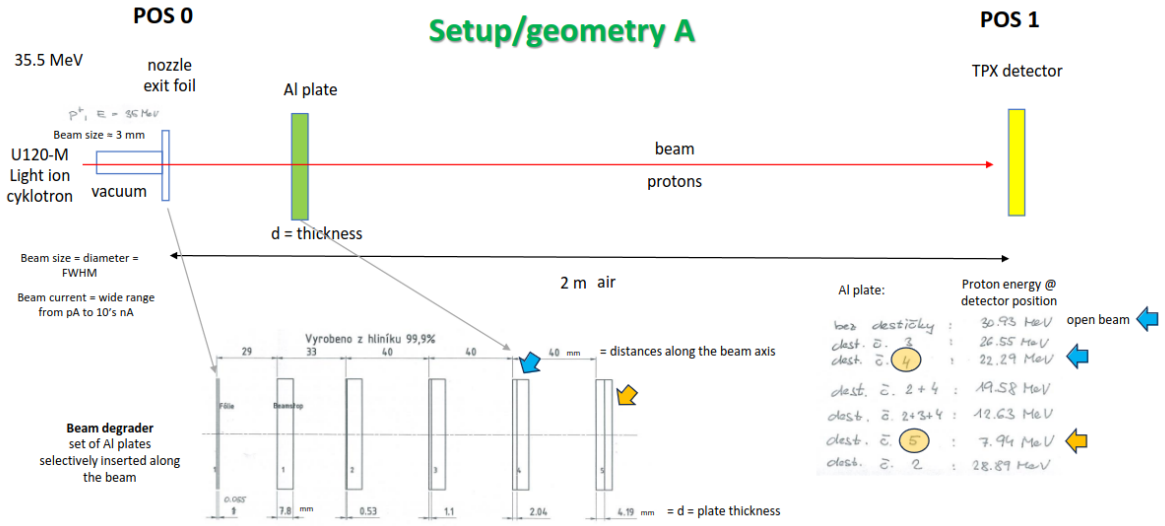

Figure 3.1: Visualisation of Cyklotron Rez setup for the experiment on 24/03/2023.

High Energy Proton Krakow Experiment (HE p Krakow)

In June 2022, another calibration experiment was performed during the High Energy Proton (HE p) experiment in Krakow. This experiment was part of a broader research study [15]. The setup featured a monochromatic proton beam with energy levels of $8\,\mathrm{MeV}$, $32\,\mathrm{MeV}$, $70\,\mathrm{MeV}$, $150\,\mathrm{MeV}$ and $225\,\mathrm{MeV}$, directed at a TPX detector positioned two metres away, with only air in between. Additionally, the detector was mounted at various angles relative to the beam direction, ranging from 0° (perpendicular) to 90°, in increments of 15°, with a few additional runs at 85° and 88°.

In practice, the setup for the HE p Krakow experiment was identical to the Cyklotron Rez setup, except that no aluminium beam degraders were used, as well as higher proton energies.

3.2.3. In-Orbit Data Collection (JoeySat/TPX Satellite Data)

The in-orbit data for this thesis was collected by a Timepix3 detector aboard the OneWeb JoeySat, a technology demonstration satellite launched in May 2023. During its initial commissioning phase, the satellite operated in a near-polar Low Earth Orbit (LEO) at an altitude of approximately 610 km. The internal TPX3 detector is situated behind the satellite's primary structure, which is modelled in this work as an equivalent of $5\,\mathrm{mm}$ of aluminium shielding. For this study, data was used from a period in March 2024, during which the detector continuously measured the internal radiation environment. The collected data provides high-resolution measurements of particle flux, deposited energy, and particle type, which forms the basis for the analysis presented in the later chapters of this thesis.

3.3. Numerical calculations, Monte Carlo simulations (Geant4)

This section describes the simulation framework which was used to simulate particle transport.

3.3.1. Geant4 tool, Radiation transport & Physics models

Geant4, an object-oriented C++ toolkit, is chosen for its flexibility in simulating particle interactions through matter. It is highly customisable, allowing for complex geometries and tailored physics processes crucial for your thesis. Geant4 boasts a large, active community, indicated by its high citation count, which ensures extensive support and validated physics models. This broad acceptance is a key advantage over some alternatives.

Geant4, a Monte Carlo-based toolkit developed by CERN, is chosen to simulate the interaction of radiation with matter. It allowed for detailed specification of geometries, materials, and particle sources. Geant4 has a large, active community and has the highest citation count of all particle transport codes. [5]

Compared to FLUKA, which is largely Fortran-based, Geant4's C++ design provides better modularity and extensibility for custom setups. This was a logical choice given the author's experience in C++. While PHITS excels in heavy ion transport, Geant4 offers a broader range of electromagnetic physics, which was useful for this thesis's focus on proton, electron, and X-ray transport. GRAS, though specialised for space applications and initially recommended, was set aside as Geant4 provided more direct options for defining geometry, physics lists, and overall setup. GRAS is still believed to be the next best option, despite initial installation difficulties. Mulassis, while useful for multilayered shielding dose calculations, was not selected as this work focuses on a single-layer shield and the effects on deposited energy, secondary particle generation, and kinetic energy reduction. [ADD sources]

The following physics lists were used in the simulations:

- `G4EmStandardPhysics`
- `G4EmLivermorePhysics`
- `G4HadronPhysicsQGSP_BIC_HP`
- `G4NeutronTrackingCut`
- `G4RadioactiveDecayPhysics`

These were selected to have correct modelling of both electromagnetic and hadronic interactions. The Livermore model was necessary to account for low-energy processes such as X-ray production, which are relevant for secondary particle generation. In addition, the physics lists G4HadronPhysicsQGSP_BIC_HP, G4NeutronTrackingCut, and G4RadioactiveDecayPhysics were included to model hadronic interactions and post-shielding particle behaviour. QGSP_BIC_HP provides accurate simulations of interactions and low-energy neutron transport. G4NeutronTrackingCut improves runtime by removing long-lived thermal neutrons. They can take a long time before being fully absorbed and have minimal impact on the detector response. G4RadioactiveDecayPhysics was included to account for having a full spectrum of secondary particle generation due to nuclear decay processes. The standard EM model alone was found to be insufficient in capturing these effects, particularly for secondary particle generation.

The `fStopAndKill` functionality in Geant4 allows for the explicit termination of a particle's tracking at a specific point, in this case when it hits the detector. This means the particle stops depositing energy and generating secondaries after that point. In this study, it was found that Geant4 simulations initially produced many secondary particles within the detector volume, which did not align with Timepix outputs. Implementing `fStopAndKill` improved this agreement, making the simulation results more comparable to the experimental data. This feature is useful for optimising runtime and focusing on specific interaction points. [Add geant4 citation]

3.3.2. Radiation Detection Setups and Geometries

The general simulation framework and physics models described above were applied to two distinct geometrical configurations. Setup A was designed to replicate the on-Earth accelerator experiments for verification and validation purposes. Setup B was developed to model the satellite detector in its operational Low Earth Orbit (LEO) environment. These two setups are detailed below.

Setup A: Accelerator Beam Calibration
To accurately reproduce the experimental conditions of the Cyklotron Rez beam calibration, a Geant4 simulation was created that closely matched the physical setup. This included defining the same world material (air), reproducing the geometry of the setup, and correctly positioning the aluminium shielding plates. Initially, the Geant4 simulations were performed using an enlarged detector area ($140\,\mathrm{mm}\times140\,\mathrm{mm}$ instead of $14\,\mathrm{mm}\times14\,\mathrm{mm}$) to increase the number of recorded particles and reduce computational time. However, this introduced different behaviour compared to the physical setup. Specifically, the larger area allowed for the inclusion of more secondary particles and wider angular spreads, which did not reflect the experimental conditions. For this reason, the simulations were rerun using the actual detector dimensions, accepting lower statistics in exchange for a more realistic comparison with measured data.
For the visualisation of the simulation, OpenGL was used. A side-view of the simulated Cyklotron setup is shown in Figure 3.2. The white rectangular box ($50\,\mathrm{cm}\times50\,\mathrm{cm}\times250\,\mathrm{cm}$) defines the world volume filled with `G4_Air`. Particles are generated with $3\,\mathrm{mm}$ FWHM at the left of the simulation box and travel in the `(0, 0, 1)` direction towards the detector placed on the right. The effect of the aluminium shielding and air on particle behaviour is visible in this visualisation (the blue line does not travel in a straight line). Scattering occurs, both in the aluminium plate and in the air. This results in deflection and energy loss, often preventing particles from reaching the detector, as can be seen in the visualisation. The track colours represent the particle charge:

- Blue: positively charged particles
- Green: neutral particles
- Red: negatively charged particles

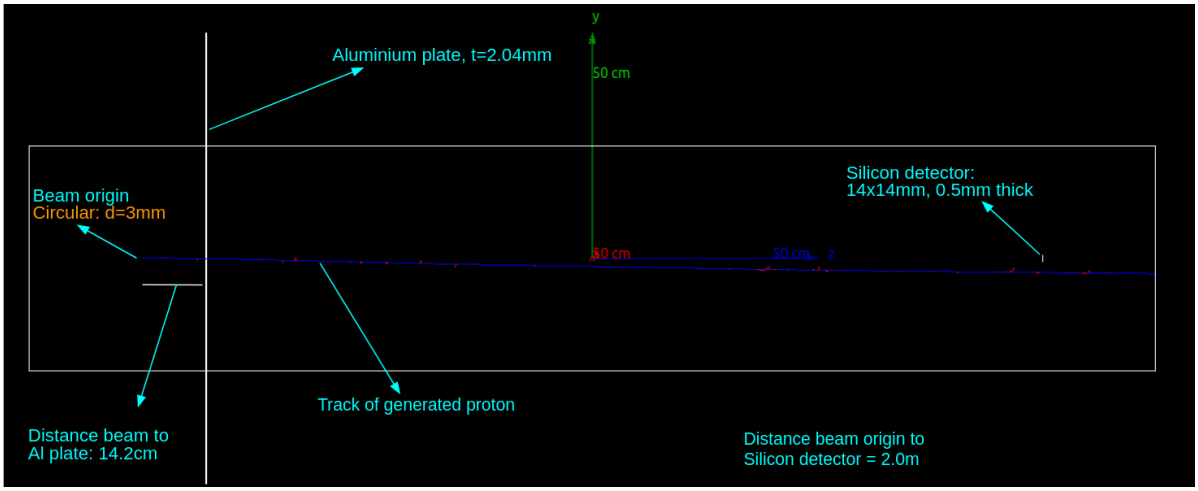

Figure 3.2: Geant4 side-view visualisation of simulated Cyklotron setup.

For the High Energy Proton (HE p) Krakow simulation, the same Geant4 setup was used as in the Cyklotron case. The only notable difference was the absence of aluminium shielding plates. Given this similarity, a separate visualisation without aluminium shielding is considered redundant and is therefore not shown here.

This setup will be referred to as Setup A in the rest of this report.

Setup B: LEO Space Environment
The simulation of the space application was created using a simplified representation of the satellite setup in Geant4. The world volume is a vacuum-filled box of dimensions $2\,\mathrm{m}\times2\,\mathrm{m}\times4\,\mathrm{m}$, defined in Geant4 as extending from $-1\,\mathrm{m}$ to $1\,\mathrm{m}$ in the x and y directions, and from $-2\,\mathrm{m}$ to $2\,\mathrm{m}$ in the z direction. This means that the $(x, y, z) = (0, 0, 0)$ is at the exact centre of this world volume. The world

volume material is `G4_Galactic`, representing a vacuum.

Near the centre of the world volume, a shielding plate is placed, with its front face at the origin $(x, y, z) = (0, 0, 0)$. This plate is made of aluminium ($5\,\mathrm{mm}$ thick) with transverse dimensions of $50\,\mathrm{cm} \times 50\,\mathrm{cm}$. Directly behind the aluminium shield, a silicon detector is positioned with its front face at $(0, 0, 5.01\,\mathrm{mm})$. This extra $0.01\,\mathrm{mm}$ is to avoid any physical overlap of shapes in Geant4 and is deemed sufficiently small to not have any effect. The detector has a thickness of $0.5\,\mathrm{mm}$ (equivalent to $500\,\mu\mathrm{m}$) and lateral dimensions of $14\,\mathrm{mm} \times 14\,\mathrm{mm}$, matching the physical properties of the Timepix3 sensor.

Looking at Figure 3.3, some features become clear.
The simulation represents an isotropic 2π hemispherical source. This source configuration was chosen for multiple reasons:

- It prevents particles from reaching the detector from behind in the absence of shielding. It is believed that little to no backscattering is present in the actual satellite setup so this simplifies the geometry and Geant4 code.
- This setup, allows the use of a flat aluminium slab instead of a more complex spherical shield as is conventional in most shielding studies.
- It more accurately reflects actual space conditions compared to a collimated beam, as particles in space arrive at varying angles. These angles significantly influence whether particles hit or miss the detector, and thus affecting the encountered energy spectrum.

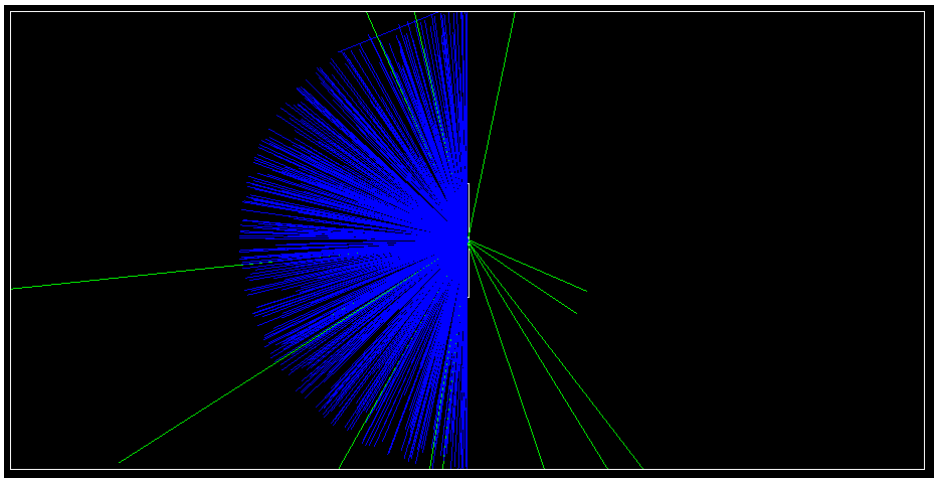

Figure 3.3: Visualisation of the setup with an isotropic 2π hemispherical source, showing 500 generated proton particles. Particles are generated isotropically within a sphere of $1\,\mathrm{m}$ and focused towards the centre (0, 0, 0). The front face of the $5\,\mathrm{mm}$ shielding is placed at this centre. The front face of the $14\,\mathrm{mm} \times 14\,\mathrm{mm} \times 500\,\mu\mathrm{m}$ detector is placed at the back of the shielding at (0, 0, $5.01\,\mathrm{mm}$). Colours represent particle type: Green = neutral, Blue = positively charged, Red = Negatively charged.

In this configuration, particles are generated isotropically from the surface of a hemisphere with a radius of $1\,\mathrm{m}$. This setup represents an isotropic source distribution over a 2π solid angle, with all particles directed towards the centre at coordinates (0, 0, 0), which corresponds to the front face of the shielding. A $5\,\mathrm{mm}$ thick aluminium shield with its front face is placed at this location. The detector is positioned just behind it at (0, 0, $5.01\,\mathrm{mm}$). The additional $0.01\,\mathrm{mm}$ offset ensures that there is no physical overlap between the shield and the detector in the Geant4 simulation.
On the right-hand side of Figure 3.3, fewer particle tracks are visible. This is because particles that hit the detector are stopped and their tracks are terminated as the `fStopAndKill` process is active (see Section 3.3.1 for details).
Backscattering is clearly visible on the left side of the figure, where green (neutral) tracks can be seen deflecting backward after interacting with the shielding. Any visible tracks on the right-hand side of the shielding represent particles that penetrated the shield but missed the detector.

This setup will be referred to as Setup B in the rest of this report.

3.4. Data Processing & Analysis

A suite of software and analytical tools was used to process, analyse, and interpret the results from experiments and simulations. This section details the initial processing of raw experimental data to the handling of simulation outputs and the application of analytical models.

3.4.1. Processing of Experimental Data

The raw data collected from the Timepix3 (TPX3) detector was preprocessed using Advacam's Data Processing Engine (DPE) [1]. This software performs several tasks like the clustering of measurements, calibration of deposited energy values, and classification of particle types based on their interaction patterns. The classification used in this study distinguishes between protons and ions, high-energy (HE) electrons, and low-energy (LE) electrons or X-rays. Preprocessed output includes histograms and spectral plots, of which the most interesting are the ones of deposited energy and Linear Energy Transfer (LET). Most of the data used in this study was received in a processed form. However, for the Krakow calibration experiment, the preprocessing steps were performed personally using the DPE tool.

3.4.2. Simulation Output Processing (ROOT Framework)

The output of the Geant4 simulations was saved in '.root' files, which were processed using the ROOT data analysis framework developed at CERN. ROOT was used for creating histograms, plotting energy distributions, and scripting the analysis in an automated format. For each particle interaction recorded in the detector, the following parameters were saved:

- **Deposited Energy:** The energy deposited by the particle in the sensor volume for a given step.
- **Kinetic Energy:** The particle's kinetic energy at the moment of detection.
- **LET:** The Linear Energy Transfer, calculated from the energy deposited per the length of the simulation step.
- **ParentID:** An integer identifier used to trace the lineage of secondary particles back to their primary source.
- **ParticleType:** The name of the particle (e.g., proton, gamma, e-).
- **fEvent:** The event number used to group all particles originating from the same primary source event.
- **isPrimary:** A boolean flag (true/false) to quickly identify if a particle is a primary particle.
- **fX, fY, fZ:** The position coordinates of the particle interaction within the detector.

3.4.3. Simplifications & Limitations of the Geant4 Simulation

Several simplifications and limitations inherent to the Geant4 simulation framework used in this work should be noted. These choices were made to maintain a manageable scope for the research, but they influence the interpretation of the results and offer directions for future work.

A primary simplification is the representation of the satellite's shielding as a single $5\,\mathrm{mm}$ flat aluminium slab. The actual JoeySat geometry is undoubtedly more complex, and as seen in the validation experiments, even small geometric changes can lead to significant differences in results. Furthermore, the simulations were performed using mono-energetic particles with an equal number of particles at each energy level. The actual proton spectrum in Low Earth Orbit is not uniform but is heavily weighted towards lower energies. A valuable direction for future work would be to fold the mono-energetic results from this study with a realistic LEO proton spectrum model, such as those from SPENVIS (ESA's SPace ENVironment Information System), to produce a more accurate prediction of the shielded environment.

There are also key differences in how the simulation records data compared to the physical Timepix3 detector. In Geant4, a "hit" is recorded for the exact pixel a particle traverses. The physical detector, however, reconstructs a particle "track" from a cluster of activated pixels. Simulating this clustering process was considered outside the scope of this research, but could be a valuable addition for future

[1] https://wiki.advacam.cz/index.php/DPE

validation efforts. This difference is also why this work focuses on particle counts and intensity rather than flux, as the concept of a collecting area over time is not directly analogous in the simulation.
The calculation of Linear Energy Transfer (LET) also presents a discrepancy. In this work, the simulated LET is calculated by dividing the deposited energy by the particle's physical step length in the sensor (‘aStep->GetStepLength()‘). This is a physically accurate definition. However, the LET provided by the TPX3 detector's post-processing is based on a more complex track reconstruction algorithm. It was observed in the validation chapter that simply normalising the deposited energy by the sensor thickness ($500\,\mu\mathrm{m}$) often provided a better, though only for perpendicular beams, alignment with the experimental data. This difference in LET calculation is a significant source of uncertainty when comparing simulated and measured results.
Finally, several avenues for enhancing the simulation's fidelity were identified but not implemented. The current simulation does not make use of the particle's angular information, which could be used to better explain discrepancies with the TPX3 data. Additionally, while it is possible to generate particles with a Gaussian energy distribution or to simulate a mixed radiation field, these complexities were set aside in favour of a more fundamental analysis using mono-energetic particles.

3.4.4. Analytical/Numerical Tools

In addition to the primary simulation and data processing software, an analytical model and a numerical database were used for energy reconstruction and validation.

Backwards Propagation Model

A backwards propagation model was implemented in Python to estimate the original kinetic energy of particles prior to traversing the shielding. The model uses the Bethe-Bloch equation to convert a measured LET value in the silicon detector into an estimate of the incident kinetic energy. It operates by stepping backwards from the detector plane through layers of material, estimating the energy at each stage.

SRIM

The SRIM (Stopping and Range of Ions in Matter) database served as a reference point for validating the backwards propagation model. It provides well-established data for the stopping power and range of protons in materials like aluminium and silicon, acting as a benchmark for the analytical model's performance.

4

Model Verification & Validation

This chapter validates the Geant4 simulation framework by comparing its predictions against data from ground-based accelerator experiments. The complete methodology, including the detailed setups of both the Cyklotron Rez and HE p Krakow experiments and the corresponding simulation model (Setup A), is described in Chapter 3.
The primary objectives of this chapter are:

- To evaluate how well the Geant4 simulation reproduces kinetic energy, deposited energy, and LET for protons across different energy regimes.
- To identify systematic offsets or discrepancies between simulated and measured data.
- To refine the simulation setup and justify methodological choices (e.g., LET calculation method, unit choices).

The following sections present the results of this validation, beginning with the low-energy proton data from the Cyklotron Rez campaign.

4.1. Validation for Low-Energy Protons (<$40\,\mathrm{MeV}$)

This section compares the Geant4 simulation against experimental data for low-energy protons, specifically the $35.5\,\mathrm{MeV}$ beam from the Cyklotron Rez experiment and the $32\,\mathrm{MeV}$ beam from the HE p Krakow experiment.
A comparison between the simulated and the experimental Cyklotron Rez results, as seen in Table 4.1, reveals an average offset of approximately $1\,\mathrm{MeV}$ in the measured kinetic energy at the detector. In all cases, the energy detected in the Cyklotron Rez experiment is higher, except for the final aluminium plate (plate 5). This suggests that less energy is absorbed in the experimental setup. This discrepancy may be attributed to differences in the properties of the simulated `G4_Air` material and the actual laboratory air (e.g., humidity and air pressure) which can influence energy loss.

Table 4.1: Comparison of kinetic energy of proton TPX data during Cyklotron Rez experiment vs the Geant4 simulation.

Energy at generator [MeV]	**Plate number [#]**	**Thickness Aluminium plate [mm]**	**Energy at detector (Geant4) [MeV]**	**Energy at detector (Cyklotron) [MeV]**
35.5	/	/	29.50	30.93
35.5	2	0.53	27.50	28.89
35.5	3	1.10	25.09	26.55
35.5	4	2.04	21.36	22.29
35.5	5	4.19	9.37	7.94

This trend is also visible in the data from the HE p Krakow experiment. For the 32 MeV protons, the simulation overestimates the deposited energy, which corresponds to an underestimation of the proton's final kinetic energy. As shown in Table 4.2 and Table 4.3, the simulated mean deposited energy is 1718 keV compared to the measured 1264 keV. Similarly, the simulated LET is 3.47 keV/µm while the measured value is 2.45 keV/µm. This systematic overestimation of energy loss in the simulation for low-energy protons is a key finding of this validation.
This systematic overestimation of energy loss by the simulation for low-energy protons is an important finding of this validation. The discrepancy is likely rooted in the complexities of modelling particle interactions near the Bragg peak, where energy loss is highly non-linear and sensitive to the specific physics models employed in Geant4. Furthermore, uncertainties in the experimental beam's energy spread or detector charge collection efficiency could also contribute to this offset.

4.2. Validation for High-Energy Protons (70-225 MeV)

To evaluate the simulation's accuracy at higher energies, this section compares the deposited energy and LET against experimental data from the HE p Krakow experiment for proton beams of 70 MeV, 150 MeV and 225 MeV.
As seen in Figure 4.1, the tracks that protons leave on the TPX detector are clearly visible. The detector was under a 60° angle to the beam. The tracks of the protons are recognised by its straight lines. Especially for the higher energies (225 MeV and 150 MeV) in Figure 4.1a, and Figure 4.1b, the tracks are narrow and straight. For 8 MeV protons, most of the remaining proton energy is deposited in the detector and the track leaves a way bigger mark on the detector.

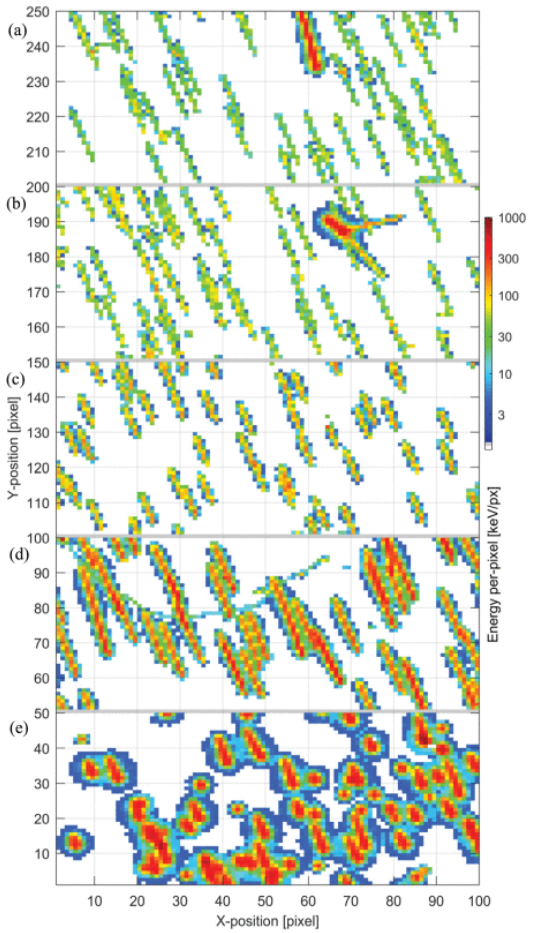

Figure 4.1: Detection by Timepix3 with a 500 µm silicon sensor of protons incident at 60° to the detector sensor plane of energies: (a) 225 MeV. (b) 150 MeV. (c) 70 MeV. (d) 32 MeV. (e) 8 MeV. Only a part of the detector pixel matrix is displayed, for each dataset 100 x 50 pixels = 5k pixels = 5.5 mm x 2.75 mm = 15.1 mm^2 = 7.6 % of the detector's total sensitive area (1.98 cm^2)[Taken from [15]]

The agreement between simulation and experiment at these higher energies is quite strong. For 150 MeV protons, shown in Figure 4.2, both the mean deposited energy and the mode bin differ by only 1 keV, indicating excellent alignment. The general shape of the spectra is also very similar.

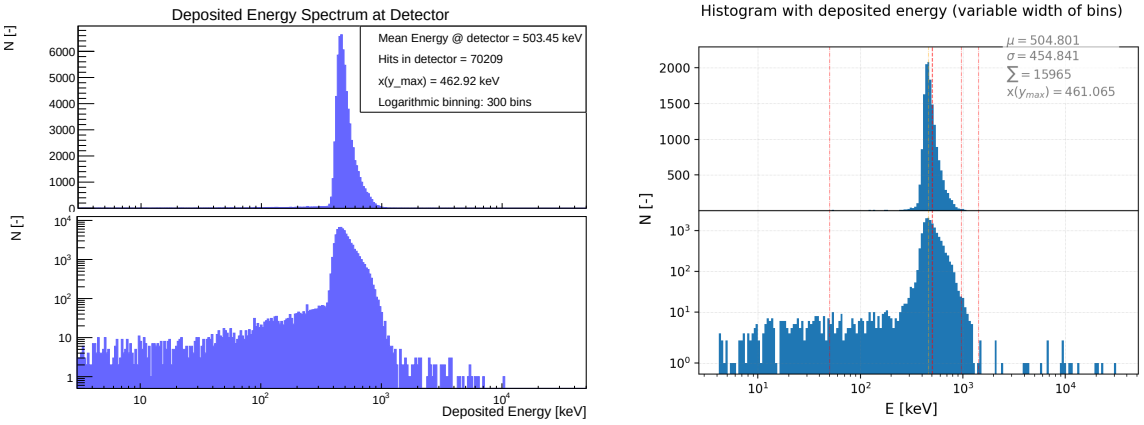

Figure 4.2: Comparison of deposited energy from Geant4 simulation and experimental data from the TPX detector. **a)** Deposited energy of all detected particles at detector for Geant4 simulation with 8×10^4 protons at 150 MeV in generator after 2 m of air, no shielding. Setup A (see Section 3.3.2). **b)** Deposited energy of protons at TPX detector for the HE p Krakow experiment 04/06/2022 150 MeV protons at 0°.

Table 4.2 and Table 4.3 provide a broader comparison. At 70 MeV, 150 MeV and 225 MeV, the agreement in both mean and modal deposited energy is strong, with the 150 MeV case being particularly well-matched. In contrast to the low-energy case, the simulation does not show a large systematic offset, suggesting it performs more reliably in this regime.

Table 4.2: Comparison of deposited energy for high-energy protons from HE p Krakow experiment vs Geant4 simulation.

Energy at generator [MeV]	Mean Edep (Geant4) [keV]	Mode bin (Geant4) [keV]	Mean Edep (TPX) [keV]	Mode bin (TPX) [keV]
70	871.6	856.81	756.70	751.04
150	503.45	462.92	504.80	461.07
225	389.88	334.79	409.64	344.06

To evaluate energy deposition more meaningfully, the Linear Energy Transfer (LET) was also compared. A consistent methodology was sought for comparing LET between the simulation and the experiment. While the Timepix3 detector's post-processing algorithm for LET is complex and based on 3D track reconstruction, it was observed that a simplified approach in the simulation, normalising the total deposited energy by the sensor's thickness (500 µm), produced results that aligned more closely with the final experimental data. This normalised LET was found to be more representative than a physically accurate LET calculated from individual particle step lengths, as the latter was artificially inflated by secondary particles with short tracks. Therefore, for the purpose of a valid comparison, this normalised LET is used for the analysis of perpendicular beam experiments. It should be noted, however, that this approach is less reliable for data involving angled particle trajectories.

Table 4.3: Comparison of LET calculation for high-energy protons from HE p Krakow experiment vs Geant4 simulation.

Energy at generator [MeV]	Mean LET (Geant4 normalised) [keV/µm]	Mean LET (TPX) [keV/µm]
70	1.76	1.491
150	1.014	0.982
225	0.785	0.793

4.3. Chapter Conclusion

The validation process detailed in this chapter confirms that the Geant4 simulation is a suitable and effective tool for the primary goals of this research. The simulation demonstrates a strong agreement with experimental data, particularly for high-energy protons, which are an important part of the radiation environment being studied.

While some systematic discrepancies were noted at lower energies, and this finding should be taken as a reason for caution when interpreting low-energy results, the overall performance of the model is considered to be within acceptable limits for the primary analysis conducted in this thesis.

Therefore, with the model's performance and limitations understood, this validation provides the necessary confidence to proceed with the main simulation and analysis in the subsequent chapters.

5

MC Simulation of space radiation in LEO orbit

This chapter discusses the Monte Carlo simulations performed to understand the effect shielding on protons, electrons and photons in a vacuum. In Section 5.1.1, the setup of this simulation will be described to recreate the shielding of OneWeb's JoeySat. Afterwards, an analysis of the effect of the shielding in terms of intensity, kinetic energy spectrum, LET spectrum, and secondary particle generation will be performed. This will serve as a foundation for the analysis of the onboard data of JoeySat.

5.1. Space Environment Simulation

In this section, the setup of the Monte Carlo simulation for the space mission in LEO will be described. Some limits of the simulation will be discussed as well in the latter part of this section.

5.1.1. Setup

The analysis of the detector's response in a space environment was conducted using the Geant4 toolkit. The simulation was configured as *Setup B*, which models the satellite's detector and shielding exposed to an isotropic radiation field similar to LEO. The complete details of the Geant4 framework, physics lists, geometry, and the isotropic source model are described in Section 3.3, with the specific geometry detailed in Figure 3.3.2. The results from this simulation are presented in the following sections.

5.2. Analysis

This section elaborates on the effect of $5\,\mathrm{mm}$ aluminium shielding on the space particles. All particles will be discussed in terms of intensity, kinetic energy and LET spectrum, and the secondary particle generation. First, the protons will be discussed for $31.7\,\mathrm{MeV}$, $32.5\,\mathrm{MeV}$, $35.0\,\mathrm{MeV}$, $40.0\,\mathrm{MeV}$, $50.0\,\mathrm{MeV}$, $100.0\,\mathrm{MeV}$ and $200.0\,\mathrm{MeV}$. Afterwards, the effect for electrons with energies of $1.0\,\mathrm{MeV}$, $3.0\,\mathrm{MeV}$, $5.0\,\mathrm{MeV}$, $10.0\,\mathrm{MeV}$ and $20.0\,\mathrm{MeV}$ will be looked at. Lastly, the photons will be analysed for energies of $20\,\mathrm{keV}$, $50\,\mathrm{keV}$, $100\,\mathrm{keV}$, $500\,\mathrm{keV}$ and $1000\,\mathrm{keV}$.

5.2.1. Protons

A range of proton energies between $31.7\,\mathrm{MeV}$ and $200\,\mathrm{MeV}$ was chosen for the simulation. It is believed that the fraction of protons with kinetic energies significantly above $200\,\mathrm{MeV}$ in Low Earth Orbit (LEO) is small, particularly in the trapped radiation environment. Additionally, the difference between the effect $100\,\mathrm{MeV}$ and $200\,\mathrm{MeV}$ protons was small enough that similar behaviour can be expected for higher energy protons.

In Table 5.1, information about the total transmission can be found about the various runs of $100\,000$ protons at different energies. Each run started with 10^5 protons, with energies corresponding to the first column in the table. The second column shows the total amount of detected particles in the detector

when there is no shielding. Due to the setup, as described before, many particles miss the detector when the shielding is removed due to the $5.01\,\mathrm{mm}$ offset between the detector and the centre of the spherical source. This is important to not compare the transmission factors with the original $100\,000$ protons but with the actual particles hitting the detector. The third column displays the total amount of detected particles in the detector after $5\,\mathrm{mm}$ of aluminium shielding. The fourth column does the same but only for the measured protons (both primaries and secondaries). Columns five and six give the total and the proton transmission percentage, respectively. Both are relative to the total detected particles without shielding as seen in column two.

Table 5.1: Total transmission of numerical results from 10^5 Protons Geant4 simulation measured at detector after 5mm Aluminium. Setup B (see Section 5.1.1)

Energy @generator	**Particles (all) in detector without shielding**	**Particles (all) in detector with 5mm Al shielding**	**Protons (primary + secondary) in detector with 5mm Al shielding**	**Total transmission %**	**Proton transmission %**
31.7 MeV	46258	1565	1	3.38%	0.0022%
32.5 MeV	46271	2680	1047	5.79%	2.26%
35 MeV	46267	14937	12975	32.28%	28.04%
40 MeV	46247	33373	30902	72.16%	66.82%
50 MeV	46233	47993	45119	103.81%	97.59%
100 MeV	46276	48412	45875	104.62%	99.13%
200 MeV	46246	48664	46158	105.23%	99.85%

Looking at Table 5.1, a clear trend can be seen: as the initial proton energy increases, both the proton-specific and the total particle transmission increase. At lower energies, such as $31.7\,\mathrm{MeV}$, the shield is highly effective, stopping virtually all primary protons. In contrast, at energies of $50\,\mathrm{MeV}$ and above, the shield becomes almost transparent to protons, with transmission rates exceeding $97\,\%$. An interesting phenomenon occurs at these higher energies, where the total particle transmission exceeds $100\,\%$, peaking at $105.23\,\%$ for $200\,\mathrm{MeV}$ protons, and possibly increasing for higher proton energies. This indicates that the shielding arrangement is generating more secondary particles than the number of primary protons it stops.

This energy-dependent behaviour is caused by the nature of proton-matter interactions. Lower energy protons have a higher probability of interaction (a larger stopping cross-section) and lose their energy more rapidly within the material, resulting in high attenuation. Higher energy protons, on the other hand, have a higher velocity and thus have less time to interact as they traverse the material. While the probability of an interaction is lower, the interactions that do occur at these high energies are energetic enough to induce nuclear reactions within the aluminium atoms. These reactions lead to the creation of secondary particle cascades, which explains why the total particle count behind the shield can exceed the initial particle count.

From these results, it can be concluded that a simple $5\,\mathrm{mm}$ aluminium shield is primarily effective for protecting against protons with energies below approximately $40\,\mathrm{MeV}$. For the higher-energy portion of the proton spectrum, the shield not only fails to stop the primary particles but also contributes to the radiation environment by generating a complex field of secondary particles. To fully characterise the effect of the shielding and the resulting radiation field, it is therefore interesting to analyse the composition of this secondary particle field. This is detailed in the following section.

In Table 5.2, this composition of the particle field behind the shielding can be seen. Once again, the kinetic energies of the protons at the generator can be found in the first column, and the total detected particles in the detector of all particles can be found in the second column. Afterwards, all the detected protons are shown. They contain both primary and secondary protons. In the fourth, fifth, sixth, and

seventh column, all the secondary electrons, photons, neutrons, and other particles can be found, respectively.

Table 5.2: Composition of Particle Field behind Shielding using Numerical results from 10^5 Protons Geant4 simulation measured at detector after 5mm Aluminium. Setup B (see Section 5.1.1)

Energy @generator	Particles (all) in detector with 5mm Al shielding	Protons (primary + secondary)	Electrons	Photons	Neutrons	Others
31.7 MeV	1565	1	24	1312	197	31
32.5 MeV	2680	1047	21	1378	201	33
35 MeV	14937	12975	26	1638	249	49
40 MeV	33373	30902	27	2037	347	60
50 MeV	47993	45119	31	2254	503	86
100 MeV	48412	45875	23	1637	779	98
200 MeV	48664	46158	24	1513	855	114

Following the analysis of the overall transmission, the composition of the particle field behind the $5\,\mathrm{mm}$ aluminium shield is presented in Table 5.2. The data once again shows relations based on the initial proton energy. At lower energies, such as $31.7\,\mathrm{MeV}$, the particle field is dominated by secondaries, with photons (gammas) constituting the largest fraction of the total detected particles. As the generator energy increases, protons become the dominant particle type, making up the bulk of the detections for energies of $35\,\mathrm{MeV}$ and above. The simulation also shows that the generation of neutrons and other secondary particles increases steadily with incident proton energy. In contrast, the number of secondary electrons remains consistently low across all simulated energies.

The physical mechanisms of particle interactions explain these observations. At lower energies, protons are more likely to be stopped by the shielding, whereas higher-energy protons can penetrate it, which explains the shift in the proton fraction. The increasing production of neutrons at higher energies is due to a greater likelihood of energetic nuclear interactions, including direct knock-on events (spallation) and the subsequent evaporation of neutrons from the excited target nucleus [27, 34]. The secondary electrons are primarily generated through inelastic Coulomb interactions with the material's atomic electrons [31].

To apply these findings to the satellite data, the characteristics of the Timepix (TPX) detector must be considered. The detector is unable to measure neutrons and has a limited, energy-dependent efficiency for detecting photons, as shown in Figure 5.1. When comparing this efficiency range (tens of keV) with the simulated kinetic energy spectrum of the secondary gammas (Figure 5.2), it is clear that the detector is effectively blind to the vast majority of these photons, which have energies in the MeV range. Given that other secondaries like electrons were found in negligible quantities, the actual experimental measurement would be almost entirely dominated by the proton flux. Therefore, for this specific experimental setup, the 'Proton Transmission %' is the more physically relevant metric for assessing the shield's performance.

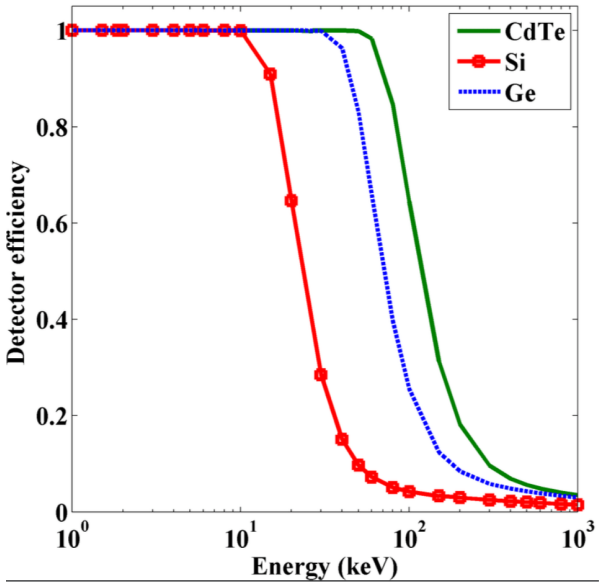

Figure 5.1: Gamma ray detection efficiency for a $500\,\mu\mathrm{m}$ thick Silicon (Si) sensor, showing the rapid decrease in efficiency for energies above $20\,\mathrm{keV}$. Based on data provided for the Timepix3 detector.

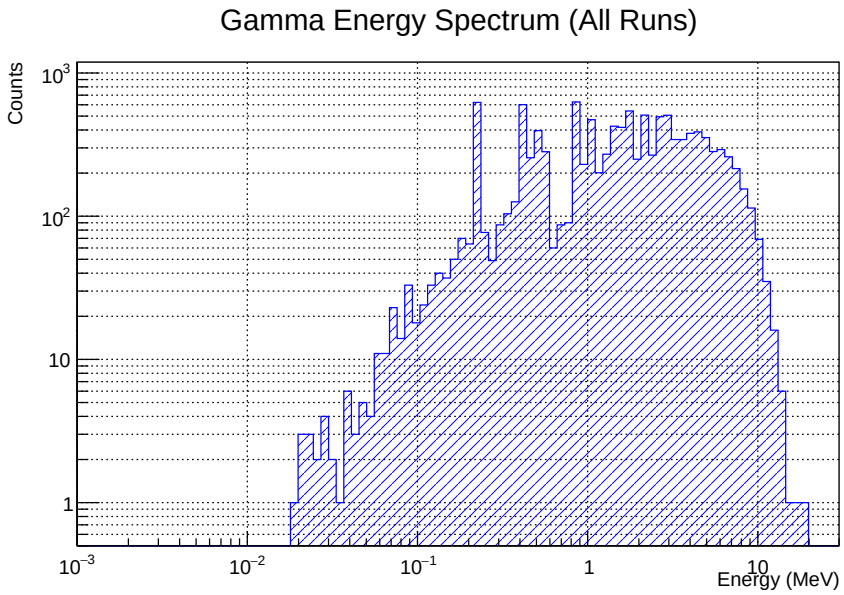

Figure 5.2: Secondary Gamma/Photon Energy Spectrum using all runs from 10^5 Protons Geant4 simulation measured at detector after 5mm Aluminium. Setup B (see Section 5.1.1). Note the scale is in MeV, and that very few photons are produced with energies below $20\,\mathrm{keV}$.

To better analyse the spatial distribution of these effects, the particle fluence or intensity on the detector is examined in Figure 5.3 to Figure 5.6.

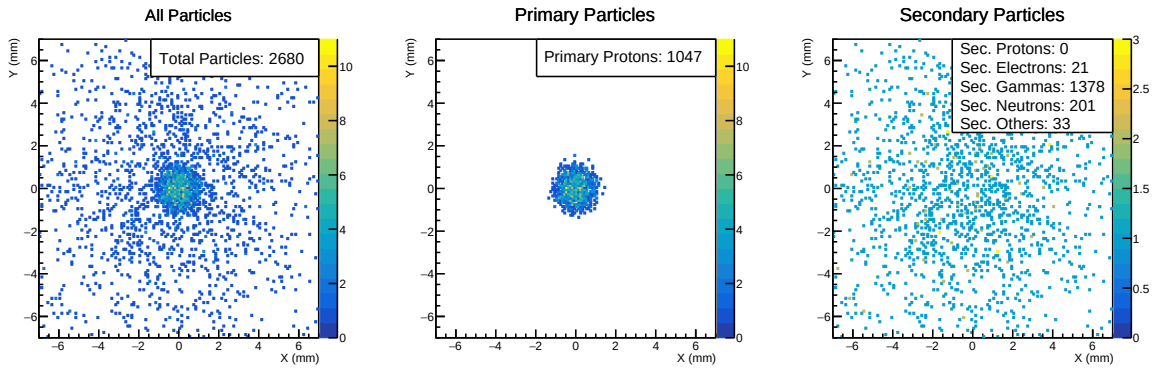

Figure 5.3: Spatial distribution of detected particles from a simulation of 10^5 primary protons. The particles were generated from an isotropic 2π hemispherical source with an energy of $32.5\,\mathrm{MeV}$ and passed through a $5\,\mathrm{mm}$ aluminium shield before reaching the $14\,\mathrm{mm}\times14\,\mathrm{mm}\times500\,\mu\mathrm{m}$ silicon detector (Setup B, Section 5.1.1). The colourbar represents the particle count per pixel.

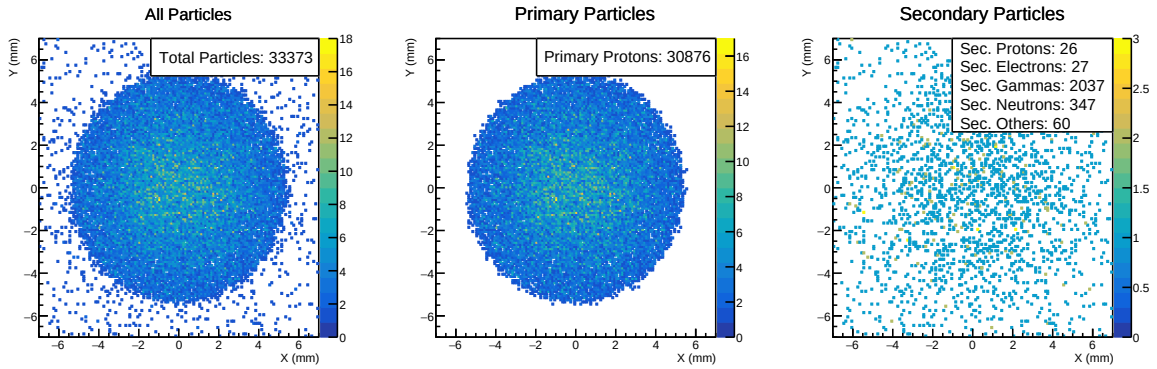

Figure 5.4: Same as Figure 5.3 for $40\,\mathrm{MeV}$ Protons

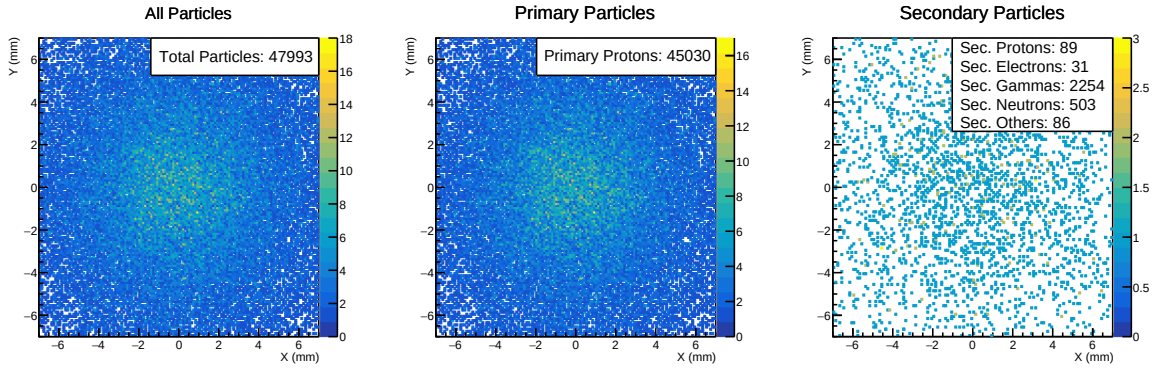

Figure 5.5: Same as Figure 5.3 for $50\,\mathrm{MeV}$ Protons

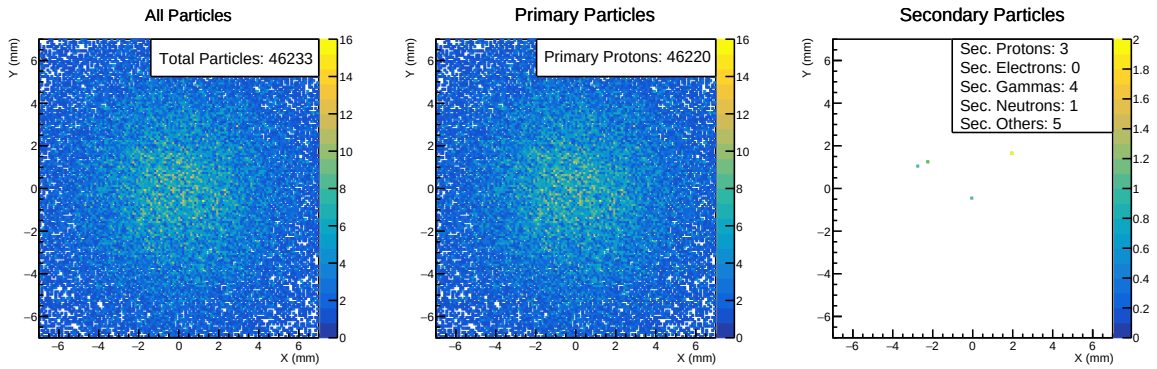

Figure 5.6: Same as Figure 5.5 for $50\,\mathrm{MeV}$ Protons WITHOUT shielding

A prominent circular pattern is evident for energies from $32.5\,\mathrm{MeV}$ to $40\,\mathrm{MeV}$, and is also noticeable at $50\,\mathrm{MeV}$ when comparing the centre of the detector to the corners. This pattern is a direct result of the simulation geometry. Protons on a perpendicular trajectory go through the minimum shield thickness of $5\,\mathrm{mm}$. Conversely, protons arriving at more oblique angles must penetrate a greater effective thickness of aluminium and are therefore more likely to be stopped. This causes a higher fluence in the central region of the detector. The unshielded reference case, shown in Figure 5.6, displays a very similar distribution, with the main difference being the additional secondary particles in the shielded scenarios. Further reference plots for all energies are available in Appendix B.

It is important to note that the simulation geometry has a dominant influence on these results. Even without shielding, positioning the detector $5\,\mathrm{mm}$ from the source centre means that only $46\,\%$ of generated particles geometrically strike the detector surface, as seen in Table 5.1. This centralised setup is also responsible for the observed circular patterns. In a real-world space environment, the radiation field is isotropic, and such a distinct pattern is not expected. Therefore, while these plots are valuable for analysing the shield's behaviour within this specific model, they do not represent an expected physical measurement. Finally, for the purposes of visualisation, the raw 256 x 256 pixel data from the detector were binned into 140 x 140 bins, yielding a plot resolution of $0.1\,\mathrm{mm}$ per bin to improve legibility.
Additionally, one should also look at the kinetic energy and deposited energy spectrum of these protons. See Figure 5.7

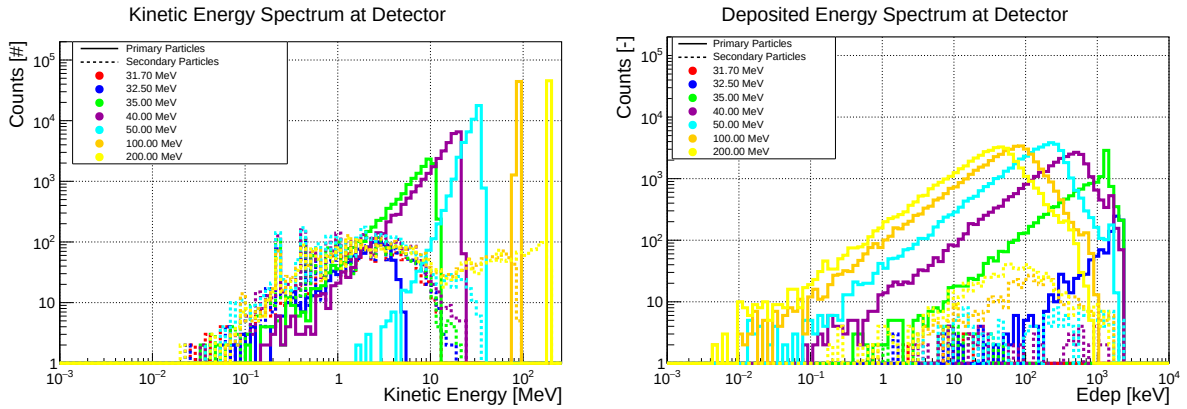

(a) Kinetic Energy Spectrum of Protons at detector.

(b) Deposited Energy Spectrum of Protons at detector.

Figure 5.7: Kinetic and Deposited Energy Spectrum from Geant4 simulation of various energy groups of 10^5 protons at detector position after $5\,\mathrm{mm}$ Aluminium shielding. Energies shown in legend correspond to generator energy for an isotropic 2π source distribution. Generated particles = 10^5 Protons, World material = G4_Galactic (vacuum), Aluminium shielding = $5.0\,\mathrm{mm}$, Setup B (see Figure 3.3.2)

When looking at the kinetic and deposited energy spectra, some important physical behaviours and trends related to the interaction of protons with the shield are revealed. For this analysis, a filter of

$E_{dep} > 0$ was applied, meaning only particles that would generate a measurable signal are included (cfr. no photons or neutrons). The presence of isolated outlier events, often corresponding to single-count bins at the extremes of the energy spectra, was noted in the data. However, as the primary goal of this analysis is to characterise the general particle behaviour, these stochastic outliers are not the focus of the subsequent discussion.[1]

The first thing to notice is that the kinetic energy distributions of protons that have traversed the $5\,\mathrm{mm}$ aluminium shield are strongly dependent to the initial beam energy.
For high-energy runs ($100\,\mathrm{MeV}$ and $200\,\mathrm{MeV}$), the primary protons show a relatively small energy spread, with clear peaks observed around $85\,\mathrm{MeV}$ and $190\,\mathrm{MeV}$, respectively. In contrast, the secondary particles generated in these runs are distributed across the entire energy spectrum below these primary peaks.
At lower incident energies ($35\,\mathrm{MeV}$ to $50\,\mathrm{MeV}$), the primary protons show a much larger energy spread. This is a consequence of the increased interactions at these energies, leading to a wider statistical variation in the energy loss experienced by each particle. Some protons pass through with minimal interaction, creating a bin of energies close to the initial generator energy, while others undergo more interactions, resulting in a broad, steady drop in counts towards lower energies.
For the $32.5\,\mathrm{MeV}$ run, only a small fraction of primary protons are transmitted, while for the $31.7\,\mathrm{MeV}$ run, a single primary proton was detected (as noted in Table 5.1), making it invisible on these spectra plots (see footnote).
The lower edge of the main distribution for primary particles is observed around $0.1\,\mathrm{MeV}$, with the secondary particle spectrum extending down to $0.02\,\mathrm{MeV}$.

The deposited energy spectra show a clear inverse relationship with the kinetic energy of the incident particles. This is expected, as particles with higher kinetic energy traverse the detector's sensitive volume more quickly, allowing less time for energy deposition via ionisation. Consequently, the E_{dep} distributions for higher E_{kin} runs are clearly shifted towards lower deposited energies.
An interesting feature across all runs is the sharp drop in measured deposited energy after around $2200\,\mathrm{keV}$. This likely corresponds to the Bragg peak for protons that have been slowed by the shield to the point of maximum energy transfer just before stopping within the detector volume.
Furthermore, the range of deposited energies widens with increasing initial kinetic energy. The $200\,\mathrm{MeV}$ run, for example, produces a deposited energy distribution spanning five orders of magnitude, from less than $0.01\,\mathrm{keV}$ to over $1000\,\mathrm{keV}$.
The effect of the $5\,\mathrm{mm}$ aluminium shield on the kinetic energy of the incident proton flux was analysed. The results, summarised in Table 5.3, were examined to determine the kinetic energy of particles reaching the detector. It was chosen to focus on the most probable (modal) energy as this best represents the expected energy of a typical transmitted particle.
A clear trend can be seen: the shield's effectiveness in reducing kinetic energy is inversely related to the initial energy of the proton. For instance, an incident beam of $35\,\mathrm{MeV}$ results in a modal kinetic energy of $9.97\,\mathrm{MeV}$ at the detector, a significant reduction. In contrast, for a high-energy $200\,\mathrm{MeV}$ beam, the modal kinetic energy is $194.39\,\mathrm{MeV}$, indicating that these highly energetic particles pass through the shield with minimal energy loss. This demonstrates that while the shield is effective at slowing or stopping lower-energy protons, its impact on high-energy primaries is less pronounced.
An important finding from this analysis is the significant energy carried by secondary particles. For the $200\,\mathrm{MeV}$ run, the mean energy of secondary particles alone is $31.13\,\mathrm{MeV}$. This shows that shielding can cause a high-energy primary radiation field to be converted into a secondary field that is, by itself, a potential hazard and more complex to characterise.

[1] For example, in the $100\,\mathrm{MeV}$ run, a single event resulted in a deposited energy of $7686\,\mathrm{keV}$. Similarly, rare events with kinetic energies lower than the main distributions were observed but are excluded from this general analysis to maintain focus on the primary trends.

Table 5.3: Numerical results of Kinetic Energy (E_{kin}) from 10^5 Protons Geant4 simulation measured at detector after 5mm Aluminium. Setup B (see Section 5.1.1)

E_{kin} **@generator [MeV]**	**Mean** E_{kin} **[MeV]**	**Mean** E_{kin} **primaries [MeV]**	**Mean** E_{kin} **secondaries [MeV]**	**Modal** E_{kin} **[MeV]**	**Modal energy reduction [MeV]**
31.7 MeV	2.59	1.42*	2.592	0.43*	31.27
32.5 MeV	2.49	2.11	2.743	2.0	30.5
35 MeV	6.71	7.33	2.614	9.97	25.3
40 MeV	13.57	14.44	2.762	20.26	19.74
50 MeV	27.14	28.69	3.457	34.13	15.87
100 MeV	84.61	89.26	12.104	91.42	8.58
200 MeV	182.98	193.54	31.125	194.39	4.61

*For the $31.7\,\mathrm{MeV}$ proton run, only one primary proton hit the detector. Therefore, these values should be interpreted with caution.

The mean deposited energy per particle, shown in Table 5.4, provides insight into the energy transfer within the detector. The results are dominated by the physics of the Bragg peak.
The highest mean deposited energy, $1360.94\,\mathrm{keV}$, is observed for the $32.5\,\mathrm{MeV}$ run. This corresponds to the initial kinetic energy in which protons have slowed sufficiently to stop within or very near the active volume of the detector, depositing their maximum energy. As the initial kinetic energy increases beyond this point (e.g., to $200\,\mathrm{MeV}$), the mean deposited energy decreases significantly to $50.34\,\mathrm{keV}$. This is a characteristic of higher energy protons which go towards the spectrum of minimum ionising particles (MIPs), which are so energetic that they traverse the detector with minimal interaction and thus deposit very little energy.

Table 5.4: Numerical results of Deposited Energy (E_{dep}) and LET from 10^5 Protons Geant4 simulation measured at detector after 5mm Aluminium. Setup B (see Section 5.1.1)

E_{kin} **@generator [MeV]**	**Mean** E_{dep} **[keV]**	**Mean** E_{dep} **primaries [keV]**	**Mean** E_{dep} **secondaries [keV/um]**	**Mean LET [keV/um]**	**Mean LET primaries [keV/um]**	**Mean LET secondaries [keV/um]**
31.7 MeV	74.22	1408.22*	13.59	2.22	50.22*	0.30
32.5 MeV	1360.94	1391.66	21.02	41.64	42.59	0.35
35 MeV	848.71	851.49	98.75	13.87	13.82	27.22
40 MeV	397.57	397.73	326.58	7.63	7.50	61.91
50 MeV	188.81	187.93	451.13	3.73	3.67	22.10
100 MeV	82.44	80.96	239.69	1.55	1.49	7.74
200 MeV	50.34	48.62	160.44	0.94	0.87	5.45

Conclusion
This analysis demonstrates that the $5\,\mathrm{mm}$ aluminium shield has a strongly energy-dependent effect on an incident proton field, which can be summarised by three key findings:

- **Intensity Reduction**: For protons with energies below $40\,\mathrm{MeV}$, the shield shows it is effective at stopping the majority of incident particles. The proton transmission rate in this regime is extremely low, with less than $3\,\%$ for protons up to $32.5\,\mathrm{MeV}$).
- **Energy Reduction**: The shield's ability to reduce the kinetic energy of transmitted protons is also most pronounced at lower energies. For instance, it reduces the energy of a $35\,\mathrm{MeV}$ proton by approximately $25\,\mathrm{MeV}$, while a $200\,\mathrm{MeV}$ proton loses less than $5\,\mathrm{MeV}$.
- **Secondary Field Generation**: For protons with energies above $50\,\mathrm{MeV}$, the shield primarily acts as a converter. It becomes largely transparent to the primary protons but generates a complex

secondary field of neutrons and photons. This effect is significant enough that the total particle count behind the shield can exceed the incident count (e.g., $105\,\%$ total transmission at $200\,\mathrm{MeV}$).

In conclusion, these findings reveal the dual nature of the shielding's interaction with protons. At low energies, it is great at reducing the kinetic energy and stopping the incident protons, whereas at high energies, it causes new risks, caused by the generation of secondary particles. To create first-order correction factors designed to reconstruct the external environment from internal measurements, it must therefore be able to account for both of these distinct physical behaviours. The data on transmission rates, energy reduction, and secondary particle composition presented in this analysis will serve as the input for the development of such a model, as seen in Chapter 6.

6

Correction of shielding to measured space radiation in LEO

This chapter will contain the results, derived from the analysis performed in Chapter 5. It will explain how radiation is affected by shielding, correction factors are derived, an application to satellite data is performed, and the limitations are discussed.

6.1. Derivation of Correction Factors

This section outlines the methodology for deriving correction factors from the simulation results presented in Chapter 5. The empirical models for these factors were established by fitting functions to the simulation data using the `scipy.optimize.curve_fit` function in Python.

6.1.1. Kinetic Energy Reduction

The first step in correcting the satellite's data is to quantify the attenuation effect of the $5\ \mathrm{mm}$ aluminium shielding on the kinetic energy of incident protons. The objective is to establish a mathematical model that relates the initial kinetic energy of a proton before it interacts with the shielding ($E_{kin_{generator}}$) to its kinetic energy upon reaching the detector ($E_{kin_{detector}}$). Such a model allows for an estimation of the external radiation field's energy spectrum based on the internal measurements.

The interaction of protons with the shielding material is a stochastic process, leading to energy straggling, as can be seen in Figure 5.7a. Consequently, a mono-energetic proton beam simulated at the exterior results in a spectrum of kinetic energies at the detector plane. To derive a deterministic relationship, the modal kinetic energy was chosen as the representative value for the post-shielding energy. This modal kinetic energy is the most frequently occurring energy in the resulting distribution. This value was determined for several initial energy points as detailed in Table 5.3.

An empirical model was developed by fitting a power law to the simulated data points. The resulting relationship between the initial (generator) and final (detector) kinetic energies is described by Equation 6.1.

$$E_{kin_{generator}} = a \cdot E_{kin_{detector}}^{b} + c \tag{6.1}$$

The optimal parameters for the fit were found to be $a = 0.276$, $b = 1.218$, and $c = 30.791$. The quality of this fit is illustrated in Figure 6.1.

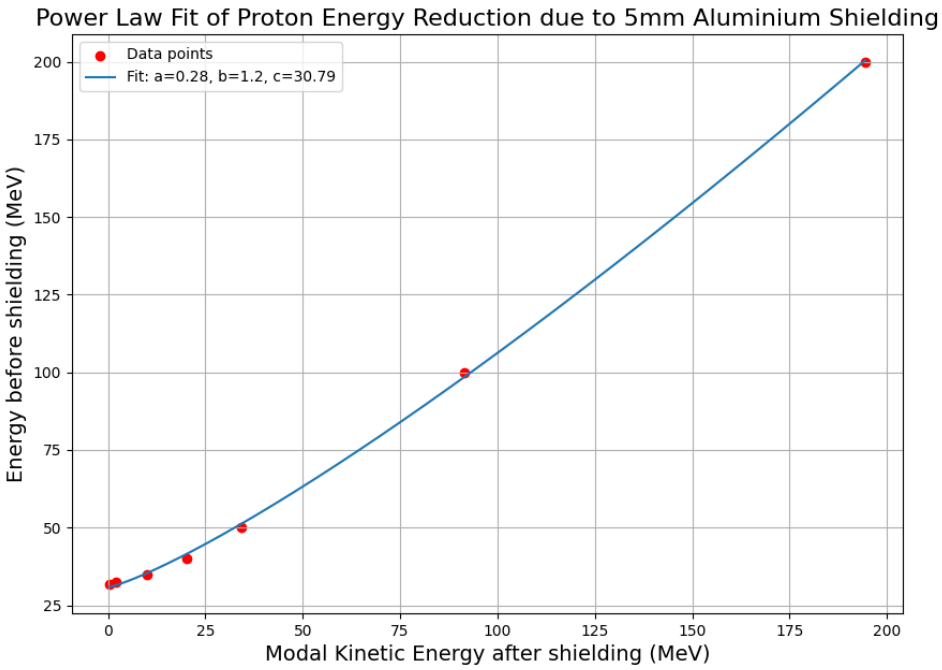

Figure 6.1: Power Law Fit for Proton Kinetic Energy Reduction due to $5\,\mathrm{mm}$ Aluminium Shielding. Correlation between incident proton energy (Y-axis, before shielding) and the corresponding modal energy detected after the shield (X-axis), based on MC Simulations.

To validate the model's predictive accuracy, the initial kinetic energies calculated using the model were compared against the known generator energies from the simulation. The results, shown in Table 6.1, demonstrate a high degree of accuracy, with a mean absolute percentage error of only 2.12% across the tested range.

Table 6.1: Comparison of Generated Kinetic Energy before shielding versus Calculated Kinetic Energy before shielding, using the power law fit with measured Kinetic Energy at detector (see Equation 6.1)

Original $E_{kin_{generator}}$ [MeV]	**Modal $E_{kin_{detector}}$ simulation [MeV]**	**Calculated $E_{kin_{generator}}$ [MeV]**	**Percentage Error [%]**
31.7	0.43	30.89	-2.56
32.5	2.0	31.43	-3.28
35	9.97	35.34	0.96
40	20.26	41.58	3.94
50	34.13	51.15	2.30
100	91.42	98.43	-1.57
200	194.39	200.38	0.19

Limitations

The model shows strong agreements, although its application is subject to certain limitations. Firstly, the derived parameters are specific to the simulated geometry, namely a $5\,\mathrm{mm}$ aluminium shield in a vacuum environment. Secondly, the model is validated for an initial energy range of $31.7\,\mathrm{MeV}$ to $200\,\mathrm{MeV}$. Protons with initial energies below $31.7\,\mathrm{MeV}$ are completely stopped by the shielding and do not reach the detector. While the trend is expected to continue for higher energies, the model's validity above $200\,\mathrm{MeV}$ has not been confirmed in this work.

The most significant challenge for applying this correction factor is its reliance on knowing the kinetic energy at the detector, a value which is not directly measured by the Timepix3 sensor. The investigation

into this issue is detailed in Section 6.2.

6.1.2. Secondary Particle Generation

An analysis of secondary particles generated by primary protons in the $5\,\mathrm{mm}$ aluminium shielding was performed to assess their potential contribution to what the detector measures. The investigation concluded that for the purpose of deriving a general shielding correction factor, their impact is negligible for the following reasons:

- **Secondary Electrons and Protons**: The flux of secondary electrons was found to be insignificant. The flux of secondary protons, while small compared to the amount of primary protons, is included in the total proton count as the detector cannot distinguish between them.
- **Secondary Photons**: While a significant flux of secondary photons is generated, their energy spectrum is predominantly in the MeV range (see Figure 5.2). This is well outside the optimal sensitivity range of the Timepix3 detector, which is most efficient for photons below $30\,\mathrm{keV}$.
- **Secondary Neutrons**: The simulation shows a non-negligible flux of secondary neutrons. However, as the Timepix3 is a direct ionisation detector, it is insensitive to neutral particles like neutrons.
- **Other Secondary Particles**: Other heavy secondary particles and ions (e.g., ^{27}Al, ^{24}Mg, deuterons) are produced. While their overall count is too low to influence a general transmission factor, these rare events may be responsible for some of the high-energy deposition noise seen in the detector data. A detailed analysis of these specific events is considered outside the scope of this work.

Given these considerations, it was concluded that it is valid to focus exclusively on the primary proton component when deriving shielding correction factors for protons for the Timepix3 detector. A more thorough analysis of secondary particles would be necessary for detectors with different sensitivities, such as those capable of neutron or high-energy photon detection.

6.1.3. Intensity Reduction (Transmission Percentage)

The second correction factor accounts for the reduction in particle intensity due to protons being stopped by or scattered away from the detector by the shielding. The objective is to establish a mathematical model relating a proton's initial kinetic energy to its probability of transmission through the shield. As this is a relative measure, this transmission percentage is equivalent to the transmission of flux or fluence, allowing for the correction of measured internal fluxes to determine the actual external flux.
As established in Section 6.1.2, the contribution from secondary particles was found to be negligible. Therefore, this analysis defines the transmission percentage as the ratio of total detected protons (both primary and secondary) at the detector with the shielding in place to the detected protons without shielding. Based on the simulation data's distribution (from Table 5.1), an inverse power law with an offset was selected as the empirical model.

$$TP(E) = \left(a - \frac{b}{E^c}\right) \times 100 \quad [\%] \tag{6.2}$$

In this model, $TP(E)$ is the transmission percentage for a given initial energy E. The parameter a was limited to a value of 1.0, as transmission cannot physically exceed 100%. The best-fit values for the remaining parameters were found to be $b = 2.48 \times 10^7$ and $c = 4.91$. Furthermore, for energies below the physical cut-off of $32.1\,\mathrm{MeV}$, where the model predicts unphysical negative values, the transmission is set to zero. The resulting fit is shown in Figure 6.2.

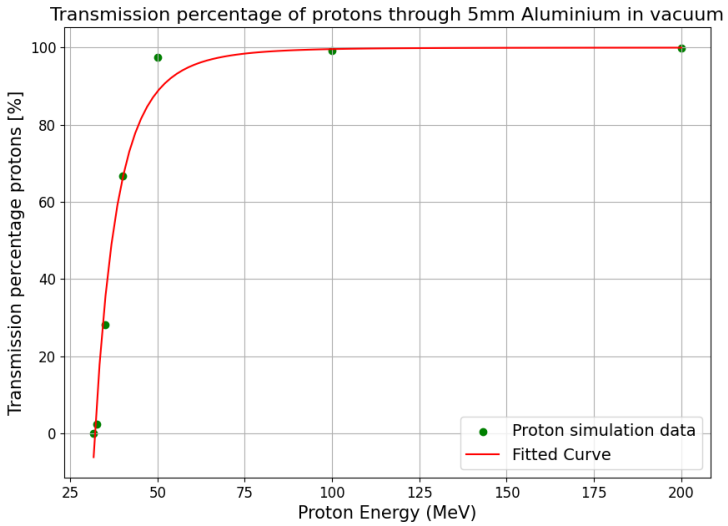

Figure 6.2: Inverse power law model fitted to the simulated proton transmission percentage through $5\,\mathrm{mm}$ of aluminium shielding, based on MC Simulations.

The model's performance was validated against the simulation data, as detailed in Table 6.2. The overall Mean Absolute Error (MAE) was found to be 2.95 percentage points, indicating a reasonable fit across the energy range.

Table 6.2: Comparison of simulated transmission percentage versus the calculated percentage from the inverse power law model (Equation 6.2).

Initial E_{kin} [MeV]	**Simulated Transmission [%]**	**Calculated Transmission [%]**	**Absolute Error [percentage points]**
31.7	0.0022	0.00	0.0022
32.5	2.26	6.02	3.76
35	28.04	34.68	6.64
40	66.82	66.09	0.73
50	97.59	88.66	8.93
100	99.13	99.62	0.49
200	99.85	99.98	0.13

Limitations

The applicability of this model is subject to several limitations. Firstly, the transmission factors are highly specific to the simulated geometry and would change with different shielding materials, thicknesses, or detector distances. Secondly, the model is only validated for initial proton energies between $32.1\,\mathrm{MeV}$ to $200\,\mathrm{MeV}$. It is hypothesised that at energies significantly higher than $200\,\mathrm{MeV}$, secondary proton generation could become so prominent that the measured transmission might exceed 100%. This is something the current model cannot reproduce due to the deliberate constraint of a 100% transmission ceiling, although it can easily be adjusted.

Finally, and most significantly, applying this correction requires the initial proton energy as an input. This means that to correct a measurement from the Timepix3 detector, one must first estimate the kinetic energy at the detector, then apply the kinetic energy correction factor to estimate the initial energy, before this transmission factor can be applied. This reliance on a chain of estimations, particularly the challenging step of converting deposited energy to kinetic energy, is a major constraint on the practical application of this correction factor.

6.2. Attempt at Converting TPX Measurements to Kinetic Energy

The primary goal of this research is to develop correction factors for the Timepix3 detector data to better characterise the external radiation field in Low Earth Orbit. It was found that an important prerequisite for applying such corrections is the ability to determine the incident kinetic energy (E_{kin}) of a particle. The detector, as such, does not directly measure E_{kin}. It measures resultant quantities such as deposited energy (E_{dep}) or post-processing calculates the Linear Energy Transfer (LET), using the estimated track length of a particle. This section describes the investigation into bridging this measurement gap, beginning with an analytical model and after performing an analysis of the energy deposition process. The initial hypothesis was that the complex LEO environment could be reasonably approximated by a simplified physical model. The first approach was therefore to model the proton flux as a perpendicular, collimated beam and develop an analytical tool to reconstruct E_{kin} from the measured LET.

6.2.1. The Backwards Propagation Method

To estimate the initial kinetic energy from detector measurements, a backwards propagation model was developed. This model uses a calibrated Bethe-Bloch formulation to work backwards from a measured LET value in the detector, through the shielding materials, to the incident energy.
The concept is formalised through the Bethe-Bloch equation, which describes the energy loss per unit distance (−dE/dx):

$$-\left\langle\frac{dE}{dx}\right\rangle = K\frac{Z}{A}\rho\frac{z^2}{\beta^2}\left[\frac{1}{2}\ln\frac{2m_e c^2\beta^2\gamma^2 T_{\max}}{I^2} - \beta^2 - \frac{\delta(\beta\gamma)}{2} - \frac{C(\beta\gamma, I)}{Z}\right] \tag{6.3}$$

- $-\left\langle\frac{dE}{dx}\right\rangle$: Stopping power [$MeV/cm$]
- $K = 4\pi N_A r_e^2 m_e c^2$: Universal constant ≈ 0.307 [$MeVcm^2/mol$]
- Z: Atomic number [-]
- A: Atomic mass [g/mol]
- ρ: Density of medium [g/cm^3]
- z: Charge of incident particle in units of e (proton = +1, electron = -1, He_4^{2+} = +2, etc.).
- β: Velocity of incident particle in terms of c [-]
- m_e = Mass of an electron
- c = speed of light
- γ: Relativistic factor = $\frac{1}{\sqrt{1-\beta^2}}$ [-]
- T_{max} Maximum energy in head-on collision = $2m_e c^2\beta^2\gamma^2/(1 + 2\gamma m_e/m + (m_e/m)^2)$ (m = mass of incident particle)
- I: Mean Excitation Potential
- $\delta(\beta\gamma)$: Density Effect Correction, for high $\beta\gamma$
- C($\beta\gamma, I$)/Z: Shell Corrections, for low β

Shell corrections and density corrections were not accounted for in this study as the energy ranges were such that these corrections are minimal.

Given a known stopping power (LET) and material properties, the particle's velocity (β) can be determined numerically. This allows for a step-by-step reconstruction of the particle's energy as it traversed the shielding in reverse. The model was first validated against the SRIM simulation toolkit, with empirical correction factors applied to ensure the LET-to-E_{kin} conversion was accurate to within 2% for relevant materials like air, silicon, and aluminium.

6.2.2. Model Success in a Perpendicular Beam Scenario

The model's performance was first tested using Geant4 simulations of a perpendicular proton beam, mimicking the conditions of a controlled experiment like the HE p Krakow setup, described in Section 3.3.2. As shown in Table 6.3, the model performed very well under these idealised conditions.

Table 6.3: Comparison of Geant4 simulation results and backwards propagation calculation results for a perpendicular beam.

Proton energy @generator [MeV]	**Measured mean LET (Geant4) @detector [keV/um]**	**Backwards calculated E_{kin} @detector [MeV]**	**Measured mean E_{kin} (Geant4) @detector [MeV]**	**Backwards calculated E_{kin} @generator [MeV]**
225	0.785	221.11	220.95 (224.11 primaries)	222.01
150	1.014	148.89	146.19 (148.84 primaries)	150.05
70	1.764	69.33	65.09 (67.94 primaries)	71.34
35.5	3.137	33.01	29.50 (31.87 primaries)	36.51
32	3.465	29.10	25.75 (28.02 primaries)	32.93

Following this successful simulation, the model was applied to the experimental data gathered during the HE p Krakow campaign. Table 6.4 presents the results of feeding the measured LET values from the TPX detector into the backwards propagation model.

Table 6.4: Comparison of TPX LET data during HE p Krakow experiment on 04/06/2022 and backwards propagation calculation results.

Proton energy @generator [MeV]	**Angle (0deg =perp)**	**LET (TPX data) [keV/um]**	**Backwards calculated Ekin @generator [MeV]**
225	0	0.79	219.73
225	30	0.85	195.60
225	60	0.85	195.60
150	0	0.98	157.71
150	30	1.10	133.53
150	60	1.08	137.05
70	0	1.46-1.49	89.69
70	30	1.84-1.87	66.92
70	60	1.87-1.92	65.47
32	0	2.40-2.45	48.59
32	30	3.30-3.38	34.19
32	60	4.19-4.23	27.29
8	0	4.18-4.30	26.99
8	30	4.91-5.01	23.69
8	60	5.21-5.31	22.62

For high-energy, perpendicular protons, the model provides a reasonable first-order approximation. For instance, at $225\,\mathrm{MeV}$ and $0°$, the reconstructed energy of $219.73\,\mathrm{MeV}$ is within 3% of the true value, closely matching the performance seen in the Geant4 simulations.
However, the data also clearly reveals the model's high sensitivity to its input LET. At $225\,\mathrm{MeV}$, a modest increase in measured LET from $0.79\,\mathrm{keV\,\mu m^{-1}}$ for $0°$ to $0.85\,\mathrm{keV\,\mu m^{-1}}$ for $30°$ and $60°$ causes

the reconstructed energy to drop by over $20\,\mathrm{MeV}$. This sensitivity means that small measurement uncertainties can produce large errors in the final result, making the model prone to mistakes due to measurement errors.
The model's performance breaks down completely at lower energies. For the $70\,\mathrm{MeV}$ and $32\,\mathrm{MeV}$ protons, the results diverge quite hard from the true values. This failure is most obvious at $8\,\mathrm{MeV}$, where the model produces a clearly wrong result of approximately $27\,\mathrm{MeV}$.
Ultimately, this analysis shows that the practical use of the analytical model is severely limited by two key factors. First, the model is highly sensitive to its LET input, where small variations in LET lead to large errors in the final calculated energy, especially for low LET values. These small variations are mainly caused by incident angles, and measurement errors. Second, the model systematically fails at low energies. A likely source for this discrepancy is the inherent imprecision in the TPX detector's own post-processing. The method it uses to estimate a particle's track length from clustered pixel data is less precise than the simulation, an effect that is likely more pronounced for the shorter, more scattered tracks of low-energy protons.

6.2.3. The Limits of the Analytical Model in a Realistic Environment

While successful in an idealised case, the goal is to apply this to satellite data. The transition from a simple beam to the complex LEO environment showed the limitations in this approach.
Firstly, the LEO radiation field is isotropic. This breaks the model's primary assumption of a fixed, perpendicular path length. A particle entering at an angle causes shifts in the measured LET for the same initial energy. This is to be expected as a particle travels through the shielding longer, loses more energy and thus deposits more energy. This leads to a higher average LET in simulations using an isotropic source, which leads to a decrease in accuracy.
Secondly, the model is based on a single LET input. Therefore, it is highly sensitive to any changes to LET. As shown with the angular data, for low LET values, any change caused large errors in the predicted kinetic energy. This makes the model's predictions fragile.
Thirdly, the TPX detector LET data shows discrepancies with the simulated data, especially at lower energies. A likely source for this discrepancy is the inherent imprecision in the TPX detector's own post-processing. The method it uses to estimate a particle's track length from clustered pixel data is less precise than the simulation, an effect that is likely more pronounced for the shorter, more scattered tracks of low-energy protons.

Knowing this and combining it with a piece of feedback during this research was the suggestion to focus on the most fundamental unit of measurement to avoid propagating errors from derived quantities, like LET. The most basic physical quantity measured by the detector is the deposited energy (E_{dep}) itself.

6.2.4. A Fundamental Analysis of Energy Deposition

The limitations of the analytical model led to a new, more fundamental research question: forgetting any specific model, is it even possible to create a reliable, unambiguous mapping from the detector's measurement (E_{dep}) to the particle's kinetic energy at the detector (E_{kin})?
To answer this, the relationship between incident kinetic energy and total deposited energy was analysed across numerous Geant4 simulations. The resulting profile plots, seen in Figure 6.3, revealed a challenging complexity. This analysis showed that for a given amount of shielding, the relationship is not a simple, one-to-one function. Instead, the data reveals that a single value of deposited energy, E_{dep}, can be produced by particles from two entirely different incident energy regimes:

1. A **high-energy particle** passing through the detector quickly, losing a small amount of energy.
2. A **low-energy particle** near the end of its track (the Bragg Peak), which slows down significantly and deposits the same amount of energy over a shorter distance.

This ambiguity is the fundamental bottleneck in this research. If a single measured E_{dep} value can correspond to multiple possible incident E_{kin} values, then no simple, direct conversion is possible.

To confirm this limitation, an empirical model was created using the profile plot from the $200\,\mathrm{MeV}$ simulation, as it covered the largest range. While the model could be constructed, when it was used to

predict the incident kinetic energy from a set of deposited energy values, the result was not a distinct energy peak. Instead, it produced a broad, scattered distribution of predicted kinetic energies.
This serves as the final confirmation: due to the underlying ambiguity in the energy deposition process, even a data-driven model fails to reliably reconstruct the incident kinetic energy.

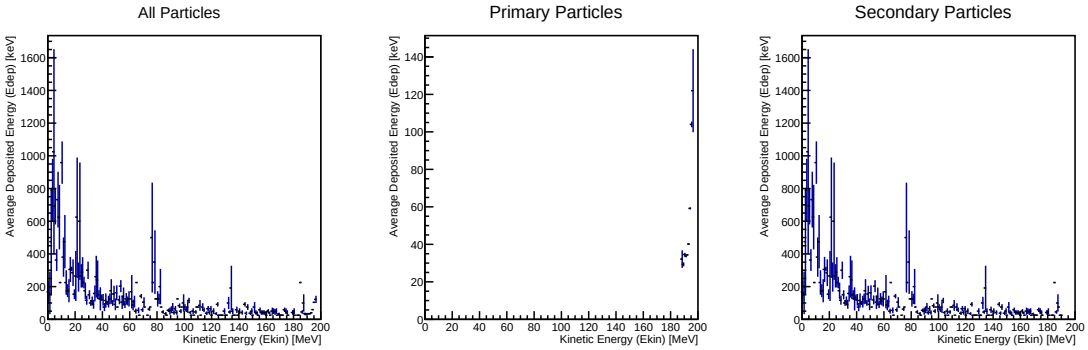

(a) The average deposited energy as a function of kinetic energy for protons originating from a $200\,\mathrm{MeV}$ isotropic 2π hemispherical source after $5\,\mathrm{mm}$ aluminium shielding.

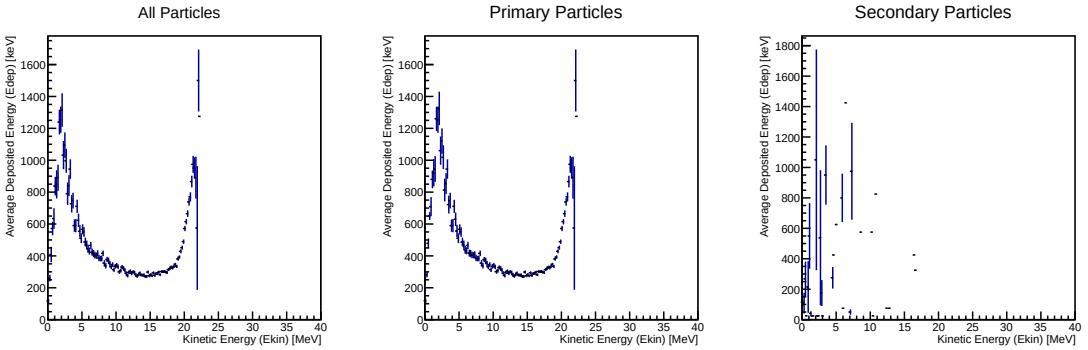

(b) Same as Figure 6.3a, for $40\,\mathrm{MeV}$.

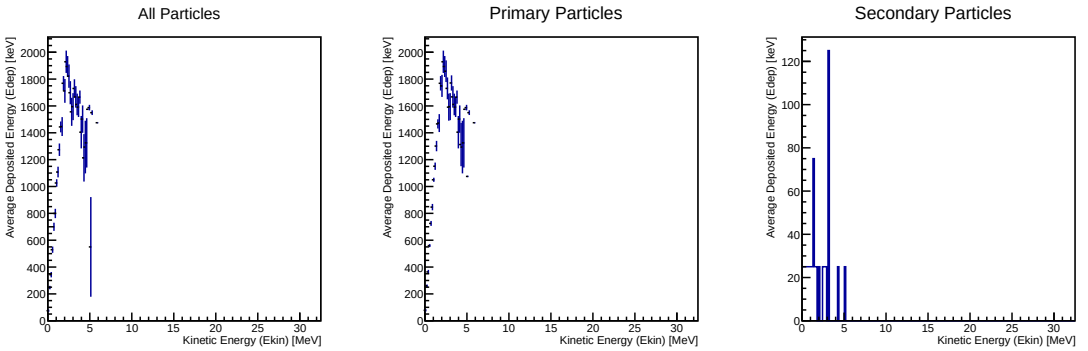

(c) Same as Figure 6.3a, for $32.5\,\mathrm{MeV}$.

Figure 6.3: Deposited energy profile versus kinetic energy in the detector for mono-energetic protons passing through $5\,\mathrm{mm}$ of aluminium shielding. The bimodal distribution in the $40\,\mathrm{MeV}$ case demonstrates the ambiguity of the energy deposition process.

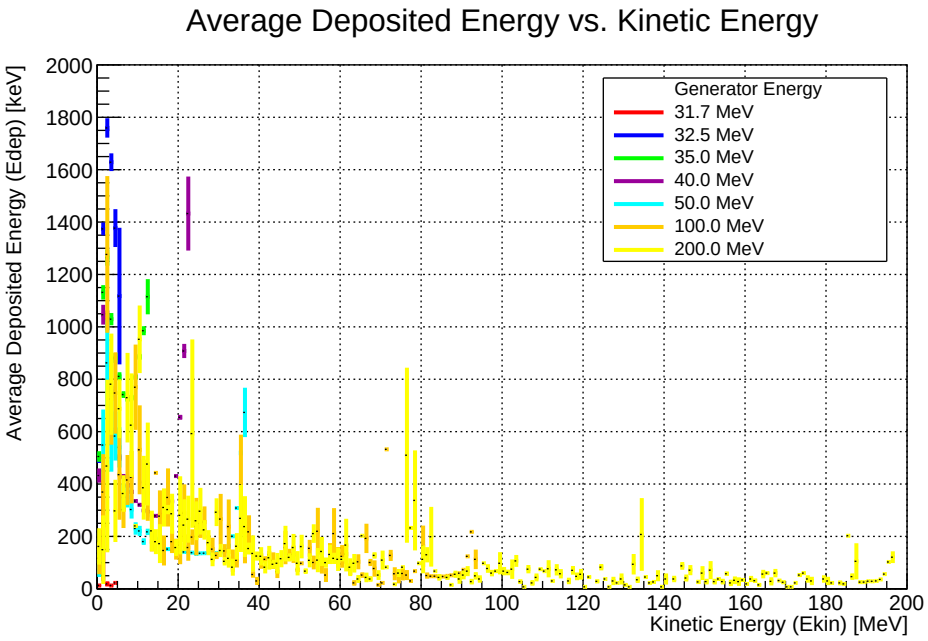

Figure 6.4: Combined Deposited Energy Profile versus Kinetic Energy in the detector for mono-energetic protons passing through $5\,\mathrm{mm}$ of aluminium shielding, using simulation data.

This is further complicated due to a discrepancy in deposited energy spectrum between the TPX measurements and the simulation data as can be seen in Figure 6.5. There are a significant amount of measurements with deposited energies in thousands of keV. This could be caused by heavy ions instead of protons, but in any case, this further complicates the issue.

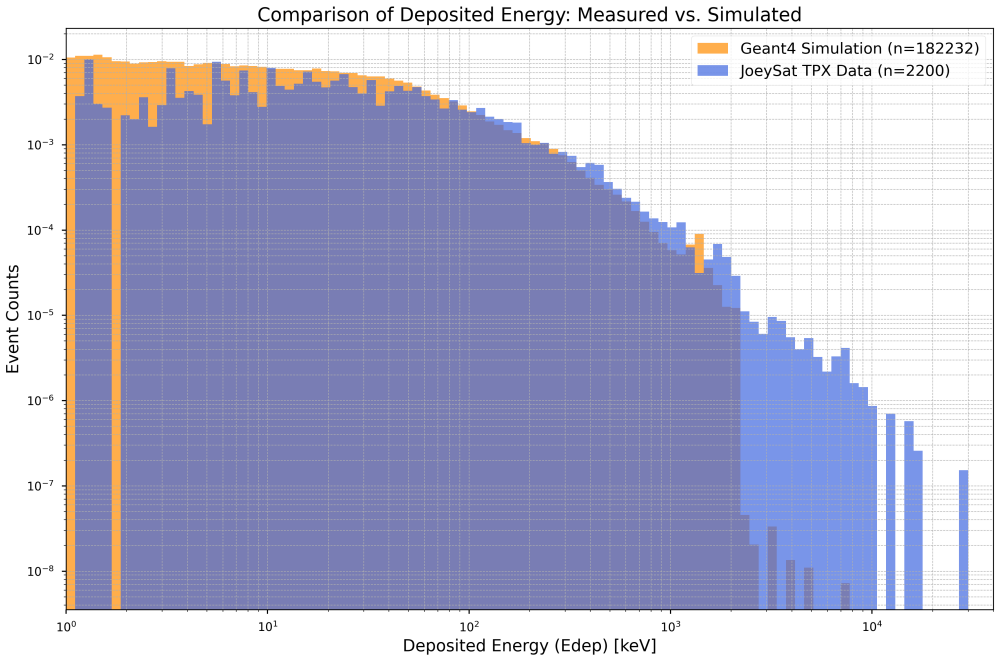

Figure 6.5: Comparison of Normalised Deposited Energy Spectrum between TPX detector (blue) and Geant4 simulation (orange) for Class 1: Protons+Ions. This spectrum contains the deposited energies for all simulated energies $31.7\,\mathrm{MeV}$, $32.5\,\mathrm{MeV}$, $35.0\,\mathrm{MeV}$, $40.0\,\mathrm{MeV}$, $50.0\,\mathrm{MeV}$, $100.0\,\mathrm{MeV}$ and $200.0\,\mathrm{MeV}$, with 5mm Aluminium. Generated particles per energy = 10^5 Protons, World material = G4_Galactic (vacuum), Aluminium shielding = 5.0mm, Setup B (see Section 5.1.1)

6.3. Discussion of Results

The analyses in this chapter successfully produced theoretical correction models, but also revealed the main challenge that currently prevents their practical application. An initial analytical model, the Backwards Propagation Method, was developed and shown to be effective for idealised, perpendicular beams. However, its limitations in a realistic, isotropic environment, coupled with a shift to using the more basic unit of deposited energy, led to more fundamental issues. This investigation revealed an inherent ambiguity in the relationship between deposited energy and incident kinetic energy. Combining this with the discrepancy in measured LET, and deposited energies is the core challenge for correcting the TPX3 satellite data. Therefore, these findings demonstrate that the correction models, while valid in principle, cannot be practically applied until the fundamental challenge of energy reconstruction is solved.

7

Conclusion

The objective of this thesis was to investigate and develop correction factors for the effects of satellite shielding on proton radiation measured by the Timepix3 detector in Low Earth Orbit. To investigate these effects, a Geant4 Monte Carlo simulation of the detector and simplified satellite geometry was developed and validated against in-beam calibration experiments which used the TPX3 detector. Although the simulations allowed these shielding effects to be quantified, the resulting models were dependent on the incident particle's kinetic energy. This is a value the Timepix3 detector cannot measure directly. It was found that reconstructing this kinetic energy from the detector's measured deposited energy outputs for a realistic isotropic radiation field is impractical. This is due to the fundamental ambiguity between a particle's deposited and kinetic energy, the unreliability of a processed unit like Linear Energy Transfer, and observed discrepancies between simulated and measured energy spectra. Therefore, while specific correction models can be created, their practical application requires first solving the fundamental problem of unambiguous energy reconstruction.

Any future attempt to create these correction factors must first overcome the specific challenges that were identified and characterised in this thesis. Recommendations for future work therefore centre on improving the fidelity of the simulation and resolving the most important discrepancies. This includes incorporating the exact satellite shielding geometry and more realistic radiation environment models, such as those provided by SPENVIS. Furthermore, research should focus on resolving the noted discrepancies between the simulated and measured deposited energy spectra. This may involve refining the post-processing of Timepix3 data and investigating the potential influence of heavy ions on deposited energy. Finally, using additional detector outputs, such as the measured particle angle of incidence, could provide a way to a more robust energy reconstruction model required for these corrections to be practically applied.

References

[1] ADVACAM (2024). MINIPIX TPX3 Datasheet.

[2] Badavi, F. F. (2014). Validation of the new trapped environment AE9/AP9/SPM at low Earth orbit. *Advances in Space Research*, 54(6):917–928.

[3] Badavi, F. F., Adams, D. O., and Wilson, J. W. (2010). On the validity of the aluminum equivalent approximation in space radiation shielding applications. *Advances in Space Research*, 46(6):719–727.

[4] Bahadori, A. A. (2024). Space radiation protection in the modern era: New approaches to familiar challenges. *Radiation Physics and Chemistry*, 221:111764.

[5] Basaglia, T., Bell, Z. W., D'agostino, D., Dressendorfer, P. V., Giani, S., Pia, M. G., and Saracco, P. (2024). Geant4: a Game Changer in High Energy Physics and Related Applicative Fields. *arXiv*.

[6] Berger, M. J. and Seltzer, S. M. (1964). Tables of energy losses and ranges of electrons and positrons.

[7] Bourdarie, S., Xapsos, M., and Member, S. (2008). The Near-Earth Space Radiation Environment. *IEEE TRANSACTIONS ON NUCLEAR SCIENCE*, 55(4).

[8] Cucinotta, F. A., Kim, M. H. Y., Willingham, V., and George, K. A. (2008). Physical and Biological Organ Dosimetry Analysis for International Space Station Astronauts. *https://doi.org/10.1667/RR1330.1*, 170(1):127–138.

[9] De Angelis, A. and Pimenta, M. (2018). *Introduction to Particle and Astroparticle Physics*. Springer, 2 edition.

[10] Dewitt, J. M. and Benton, E. R. (2020). Shielding effectiveness: A weighted figure of merit for space radiation shielding. *Applied Radiation and Isotopes*, 161:109141.

[11] DeWitt, J. M. and Benton, E. R. (2024). Secondary proton buildup in space radiation shielding. *Life Sciences in Space Research*, 41:119–126.

[12] Durante, M. and Cucinotta, F. A. (2011). Physical basis of radiation protection in space travel. *Reviews of Modern Physics*, 83(4):1245.

[13] Fourie, L. F., Square, L., Arendse, C., and Msimanga, M. (2023). ABPBI/MWCNT for proton radiation shielding in low earth orbit. *APL Materials*, 11(7).

[14] Granja, C. (2024). Presentation at the RADSHIELD Workshop. In *RADSHIELD Workshop*.

[15] Granja, C., Solc, J., Gajewski, J., Rucinski, A., Stasica, P., Rydygier, M., Marek, L., and Oancea, C. (2024). Composition and Spectral Characterization of Mixed-Radiation Fields with Enhanced Discrimination by Quantum Imaging Detection. *IEEE Transactions on Nuclear Science*, pages 1–1.

[16] Gussenhoven, M. S., Mullen, E. G., and Brautigam, D. H. (1994). Near-earth radiation model deficiencies as seen on CRRES. *Advances in Space Research*, 14(10):927–941.

[17] Hathaway, D. H. (2010). The solar cycle. *Living Reviews in Solar Physics*, 7(1):1–65.

[18] Haug, E. (2003). Proton-electron bremsstrahlung. *Astronomy & Astrophysics*, 406(1):31–35.

[19] Held, K. D. (2020). Space Radiation: An Overview. *Handbook of Bioastronautics*, pages 1–5.

[20] Heristchi, D. (1986). Hard X-Ray and Gamma-Ray Bremsstrahlung Production by High-Energy Protons in Solar Flares. *ApJ*, 311:474.

[21] Hess, W. N. (1962). Energetic particles in the inner Van Allen belt. *Space Science Reviews*, 1(2):278–312.

[22] Heynderickx, D. (2002a). Radiation belt modelling in the framework of space weather effects and forecasting. *Journal of Atmospheric and Solar-Terrestrial Physics*, 64(16):1687–1700.

[23] Heynderickx, D. (2002b). Review on modelling of the radiation belts. *International Journal of Modern Physics A*, 17(12-13):87–96.

[24] Howard, J. W., J. and Hardage, D. M. (1999). Spacecraft Environments Interactive: Space Radiation and Its Effects on Electronic System.

[25] Katsumura, Y. and Kudo, H. (2018). Interactions Between Radiation and Matter. In *Radiation Applications*, pages 7–14. Springer, Singapore.

[26] Kónya, J. and Nagy, N. M. (2012). Interaction of Radiation with Matter. In *Nuclear and Radiochemistry*, chapter 5, pages 83–129. Elsevier Science.

[27] Lechner, A. (2018). Particle Interactions with Matter. *Beam Injection, Extraction and Transfer*, 5.

[28] Mewaldt, R. A. (2007). Solar Energetic Particle Composition, Energy Spectra, and Space Weather. *Space Science Reviews*, 124:303–316.

[29] Mitchell, E. F. (2013). *Development of a miniaturised paticle radiation monitor for Earth orbit*. PhD thesis, Imperial College London, London.

[30] Montesinos, C. A., Khalid, R., Cristea, O., Greenberger, J. S., Epperly, M. W., Lemon, J. A., Boreham, D. R., Popov, D., Gorthi, G., Ramkumar, N., Jones, J. A., and Schulze-Makuch, D. (2021). Space Radiation Protection Countermeasures in Microgravity and Planetary Exploration. *Life*, 11(8).

[31] Mott, J. H. L. and Daniel, J. M. (2021). Interactions of Electromagnetic Radiation and Subatomic Particles with Matter - Part 2. *Clinical Oncology*, 33:455–460.

[32] Naito, M., Kodaira, S., Ogawara, R., Tobita, K., Someya, Y., Kusumoto, T., Kusano, H., Kitamura, H., Koike, M., Uchihori, Y., Yamanaka, M., Mikoshiba, R., Endo, T., Kiyono, N., Hagiwara, Y., Kodama, H., Matsuo, S., Takami, Y., Sato, T., and Orimo, S. i. (2020). Investigation of shielding material properties for effective space radiation protection. *Life Sciences in Space Research*, 26:69–76.

[33] NCRP (2014). Commentary #23: Radiation Protection for Space Activities: Supplement to Previous Recommendations. *National Council on Radiation Protection and Measurements*, 23.

[34] Newhauser, W. D. and Zhang, R. (2015). The physics of proton therapy. *Physics in Medicine & Biology*, 60(8):R155.

[35] of Sciences, N. A. and Medicine, E. (2018). *Testing at the Speed of Light: The State of U.S. Electronic Parts Space Radiation Testing Infrastructure*. The National Academies Press, Washington, DC.

[36] Ozsimsek, S. and Onal, M. (2019). Radiation Analysis of HR Electro-Optical Satellite. *Proceedings of 9th International Conference on Recent Advances in Space Technologies, RAST 2019*, pages 335–338.

[37] Palani Selvam, T., Shrivastava, V., and Chinnaesakki, S. (2024). Interaction of Ionizing Radiation with Matter. In Kumar Aswal, D., editor, *Handbook on Radiation Environment, Volume 2*, volume 2, pages 77–118. Springer, Singapore, Mumbai.

[38] Poivey, C. (2019). RADIATION EFFECTS IN SPACE ELECTRONICS 6 th EIROforum School on Instrumentation.

[39] Pugliese, M. (2021). Passive shielding for human space exploration. *2021 IEEE 8th International Workshop on Metrology for AeroSpace (MetroAeroSpace)*, pages 536–540.

[40] Reitz, G. and Hellweg, C. E. (2018). Space Radiation and its Biological Effects. In Bolton, P. R., Parodi, K., and Schreiber, J., editors, *Applications of laser-driven particle acceleration*, chapter 14. Boca Raton : CRC Press, Taylor & Francis Group.

[41] Simpson, J. A. (1983). Elemental and isotopic composition of the galactic cosmic rays. *Annu. Rev. Nucl. Sci.; (United States)*, 33:1:323–381.

[42] Spillantini, P. (2014). Manned exploration and exploitation of solar system: Passive and active shielding for protecting astronauts from ionizing radiation-A short overview. *Acta Astronautica*, 104(2):509–515.

[43] Spillantini, P., Casolino, M., Durante, M., Mueller-Mellin, R., Reitz, G., Rossi, L., Shurshakov, V., and Sorbi, M. (2007). Shielding from cosmic radiation for interplanetary missions: Active and passive methods. *Radiation Measurements*, 42(1):14–23.

[44] Townsend, L. W. (2021). Space Radiation Environment. In *Handbook of Bioastronautics*, pages 335–346. Springer International Publishing.

[45] Turner, J. E. (2004). Interaction of ionizing radiation with matter. *Health Physics*, pages 228–252.

[46] U. J. Nwankwo, V., N. Jibiri, N., and T. Kio, M. (2020). The Impact of Space Radiation Environment on Satellites Operation in Near-Earth Space. *Satellites Missions and Technologies for Geosciences*.

[47] Washburn, S. A., Blattnig, S. R., Singleterry, R. C., and Westover, S. C. (2015). Active magnetic radiation shielding system analysis and key technologies. *Life Sciences in Space Research*, 4:22–34.

[48] Ya'acob, N., Zainudin, A., Magdugal, R., and Naim, N. F. (2017). Mitigation of space radiation effects on satellites at Low Earth Orbit (LEO). *Proceedings - 6th IEEE International Conference on Control System, Computing and Engineering, ICCSCE 2016*, pages 56–61.

[49] Zeitlin, C. (2021). Space Radiation Shielding. In *Handbook of Bioastronautics*, pages 353–375. Springer International Publishing.

[50] Zicai, S., Yan, X., Yuming, L., Yigang, D., and Chunqing, Z. (2019). Protection of Materials from Space Radiation Environments on Spacecraft. *IOP Conference Series: Materials Science and Engineering*, 585(1):012089.

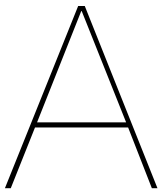

Explanation of code

This appendix provides a brief overview of the custom software and scripts developed for this thesis. The code is organised into two main projects: the primary Geant4 simulation for shielding analysis and the validation simulation.

A.1. Overview and Access

The complete source code for both projects is publicly available on GitHub to allow for transparency and future use by other researchers.

- **Primary Simulation (Thesis_V2):** This repository contains the Geant4 application used for the main analysis of shielding effects in a LEO environment.

  `https://github.com/Onnovds/Thesis_V2`

- **Validation Simulation (Thesis_V2_validation):** This repository contains the Geant4 application used to validate the simulation against ground-based experimental data.

  `https://github.com/Onnovds/Thesis_V2_validation`

A.2. Dependencies

To compile and run these simulations, the following software environment is required:

- A C++ compiler (e.g., GCC, Clang)
- Geant4 (Version 11.1 or later)
- ROOT Data Analysis Framework (Version 6.26 or later)
- Python 3.x for any analysis scripts (e.g., the Backwards Propagation Model)

A.3. Code Structure

The Geant4 applications in both repositories follow a standard structure, based on the YouTube videos from PhysicsMatters

`https://www.youtube.com/watch?v=Lxb4WZyKeCE&list=PLLybgCU6QCGWgzNYOV0SKen9vqg4KXeVL`

The key custom-written files are:

- `Construction.cc`: Defines the geometry of the simulation, including the detector and shielding materials.

- `Detector.cc`: Defines what the sensitive detector measures in the simulation and what it saves.
- `Generator.cc`: Defines the particle source (e.g., mono-energetic beam or isotropic hemisphere, energies, particle type, etc.).
- `Physics.cc`: Specifies the physics models used for particle interactions.
- `Run.cc`: Manage the data output and saving to ROOT files.
- `Satellite_test.cc` or `Project_test.cc`: The main file that initialises all other components (geometry, physics, actions) and executes the Geant4 simulation run. By typing in ./$satellite\_test.cc$ (or ./$project\_test.cc$) inside the build directory, one can run the simulation.

B

Extra results

This annex contains some supplementary figures intended to support and demonstrate the results presented in the main body of this thesis. The plots in this annex provide additional examples of analyses, such as the effect of shielding on particle intensity, performed for a wider range of initial conditions than could be included in the main chapters. Each figure caption specifies the unique parameters for that plot.

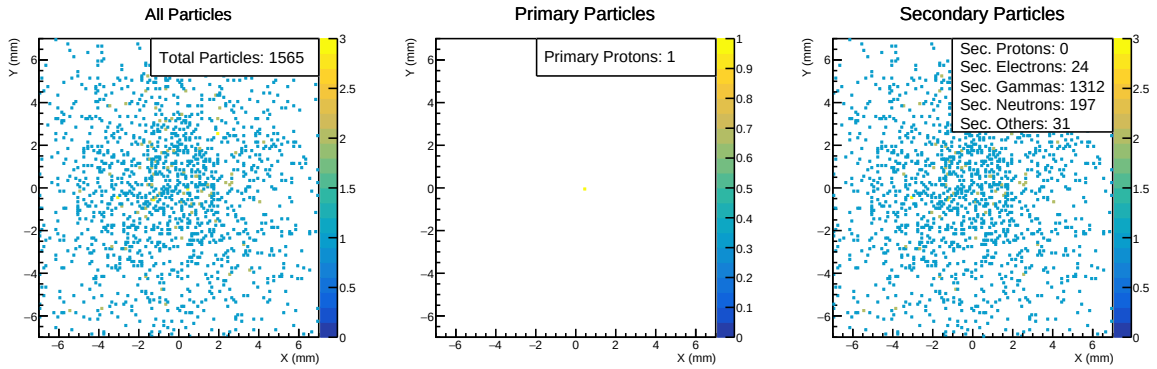

Figure B.1: Spatial distribution of detected particles from a simulation of 10^5 primary protons. The particles were generated from an isotropic 2π hemispherical source with an energy of $31.7\,\mathrm{MeV}$ and passed through a $5\,\mathrm{mm}$ aluminium shield before reaching the $14\,\mathrm{mm}\times14\,\mathrm{mm}\times500\,\mu\mathrm{m}$ silicon detector (Setup B, Section 5.1.1). The colourbar represents the particle count per pixel.

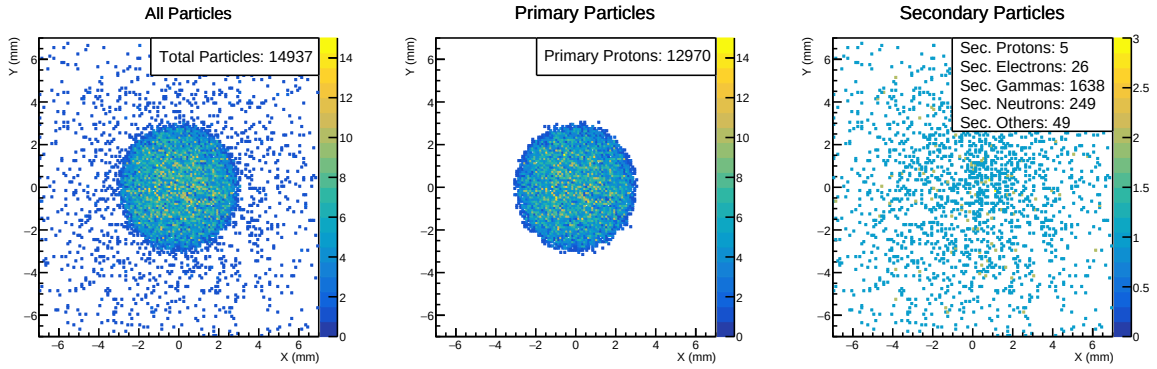

Figure B.2: Same as Figure B.1 for 35 MeV Protons

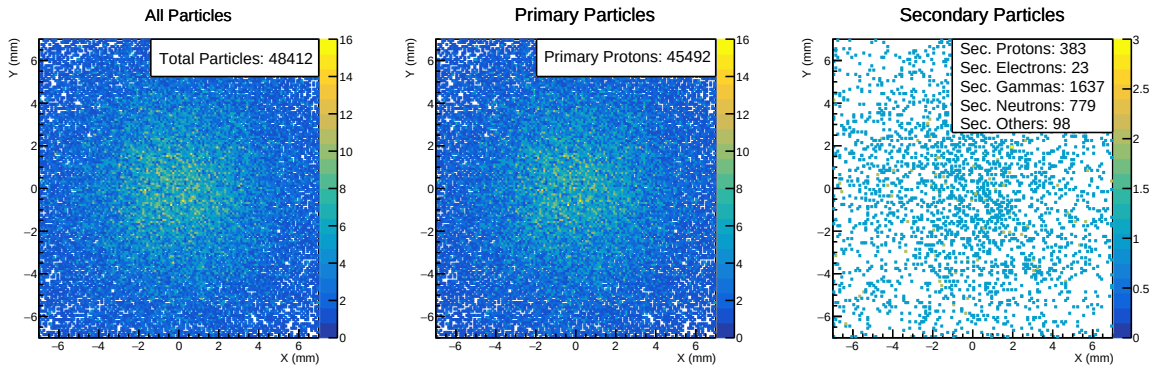

Figure B.3: Same as Figure B.1 for 100 MeV Protons

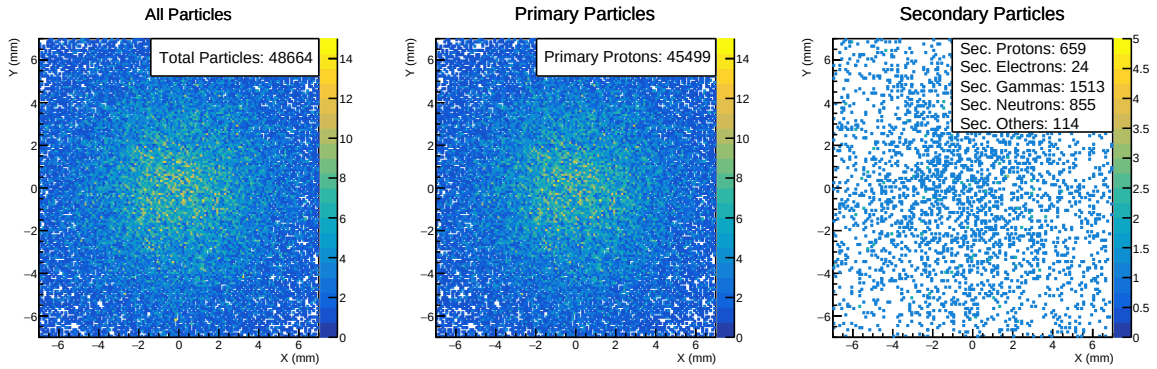

Figure B.4: Same as Figure B.1 for 200 MeV Protons

Extra proton plots without shielding:

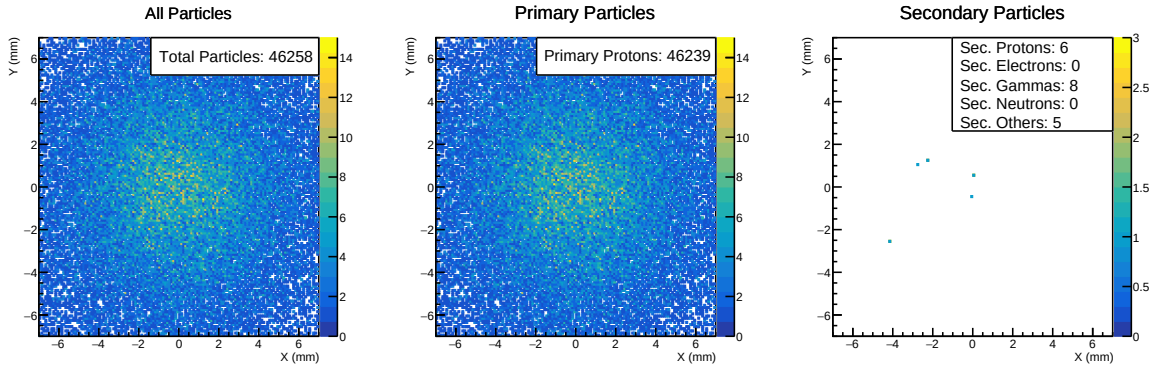

Figure B.5: Same as Figure B.1 for 31.7 MeV Protons WITHOUT shielding

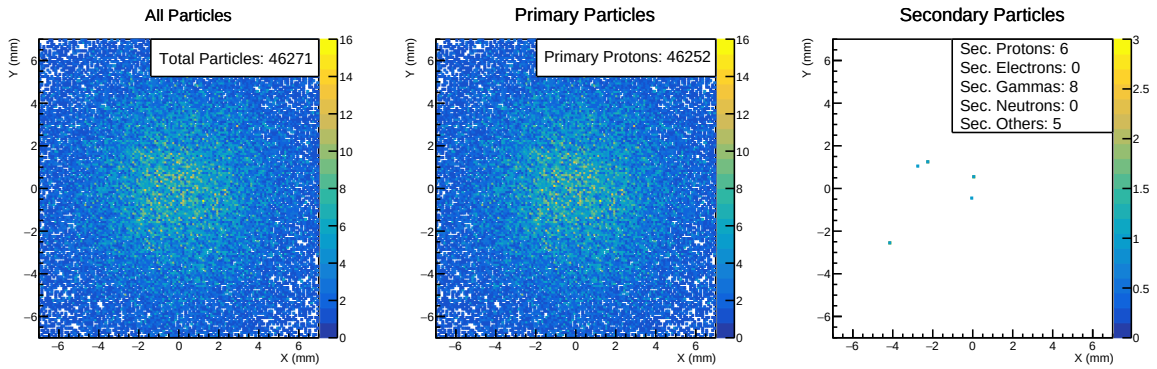

Figure B.6: Same as Figure 5.3 for 32.5 MeV Protons WITHOUT shielding

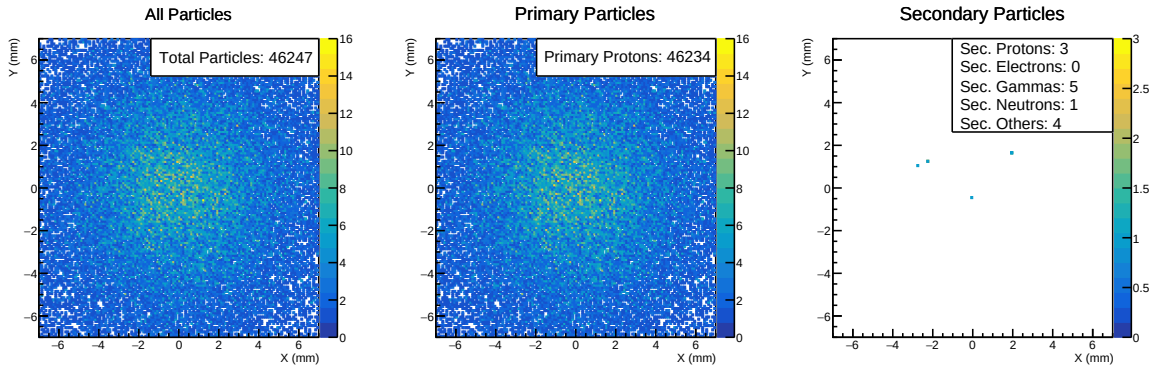

Figure B.7: Same as Figure 5.4 for 40 MeV Protons WITHOUT shielding

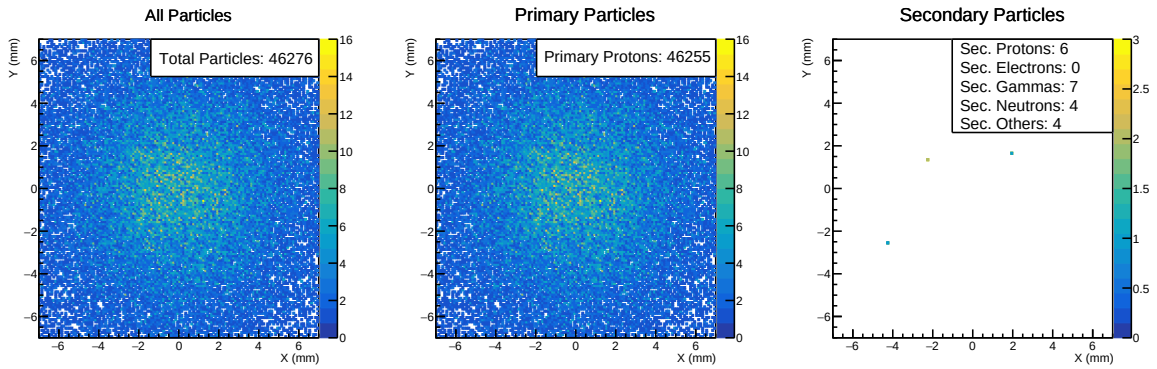

Figure B.8: Same as Figure B.3 for 100 MeV Protons WITHOUT shielding

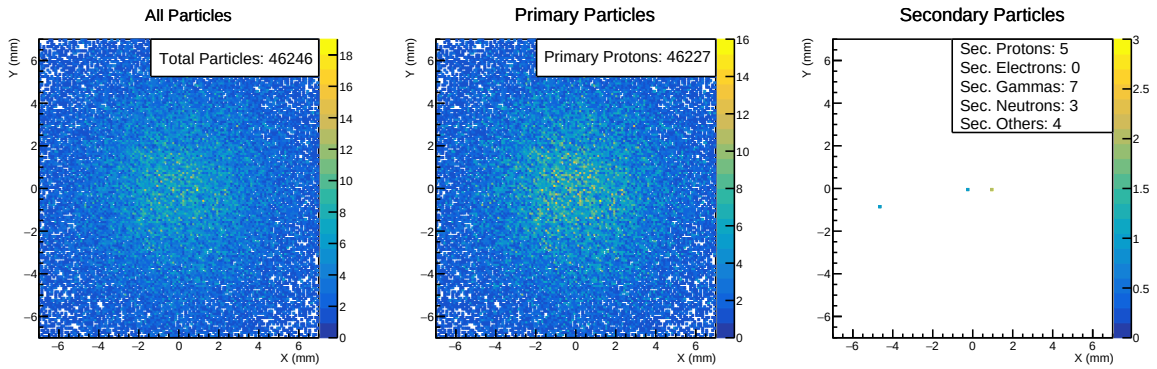

Figure B.9: Same as Figure B.4 for 200 MeV Protons WITHOUT shielding

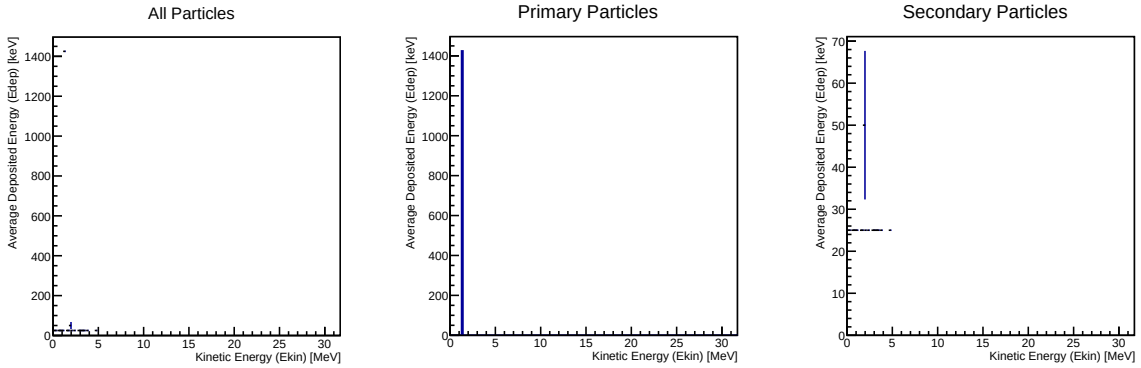

Figure B.10: The average deposited energy as a function of kinetic energy for protons originating from a $31.7\,\mathrm{MeV}$ isotropic 2π hemispherical source after $5\,\mathrm{mm}$ aluminium shielding.

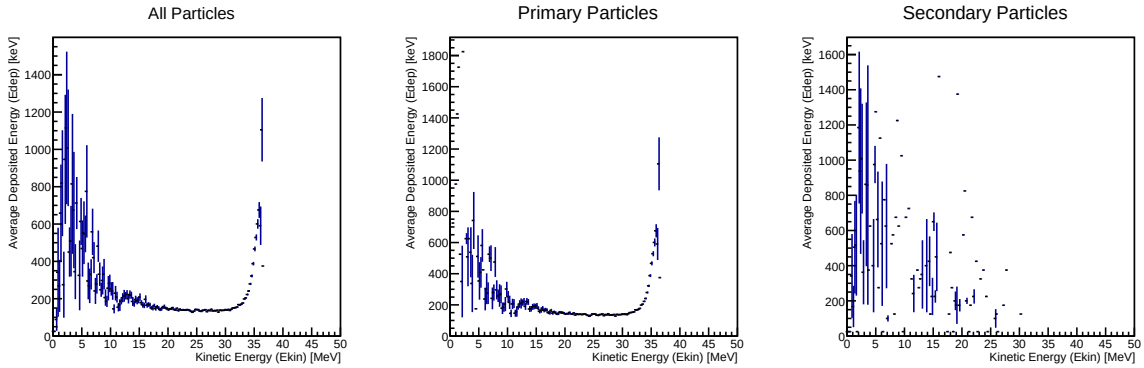

Figure B.11: Same as Figure B.10 for $50\,\mathrm{MeV}$

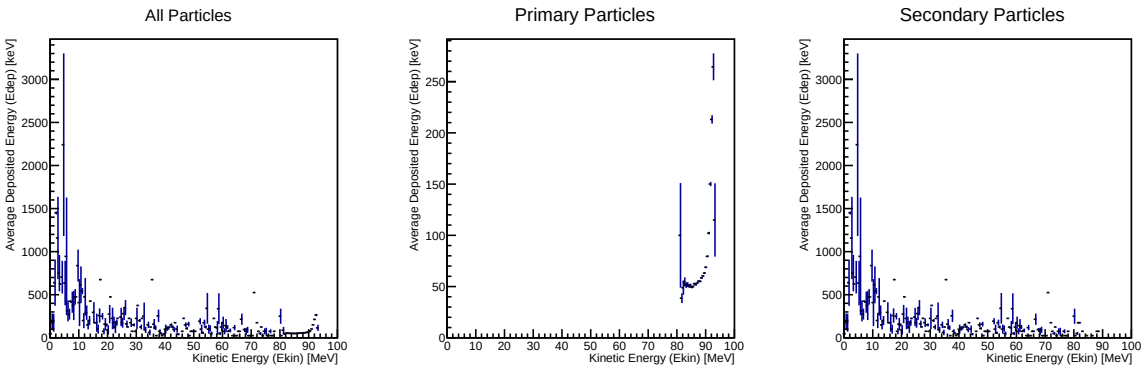

Figure B.12: Same as Figure B.10 for $100\,\mathrm{MeV}$

C

Further Physics Framework

This appendix provides supplementary background information to support the theoretical concepts discussed in the main body of the thesis. It includes a more detailed discussion of the primary sources of the space radiation environment in Low Earth Orbit, the specific effects of radiation on biological and electronic systems, and the underlying physics of particle interactions with matter. The material presented here is intended to offer a deeper context for the interested reader.

C.1. Space Radiation Environment in LEO

In the Low Earth Orbit (LEO) environment, there are three sources of radiation that have effects on spacecraft and humans: Solar Energetic Particles (SEPs), Galactic Cosmic Rays (GCRs), and Trapped Particles. In this Section, these types will be discussed one by one in terms of their origin, the types of particles they contain, their energies and certain specifics. Insights about the influence of the Sun and Earth's magnetic field can be found in Appendix C.

C.1.1. Solar Energetic Particles

Solar Energetic Particles (SEPs) are high-energy particles primarily generated by solar events such as solar flares and coronal mass ejections (CMEs), which stem from magnetic instabilities in the Sun's corona [7]. The composition of SEPs is mainly protons, with a smaller fraction of heavier ions and electrons, and their energies can exceed 1 GeV, although SEPs generally have lower energies than GCRs, which is discussed in Section C.1.2 [4]. SEPs have kinetic energies ranging from about $1\,\mathrm{MeV}$ to several hundred MeV, depending on the intensity and origin of the solar event [19].

SEPs are typically classified by the type of solar event responsible for their generation. Solar flares, characterised by brief, intense emissions, produce impulsive SEPs that are rich in electrons. In contrast, CMEs, which are large expulsions of plasma and magnetic field from the Sun's corona, produce gradual SEPs with a proton-heavy composition [44]. Additionally, the sun emits the solar wind, a steady, low-energy flow of particles (mainly protons and electrons) with velocities between 400 km/s and 800 km/s which provides a constant background, though it usually does not significantly impact spacecraft operations except for minor surface charging effects [29].

Solar Particle Events (SPEs) broadly refer to these high-energy emission events from the Sun, with Solar Proton Events (abbreviated as SPEs) indicating specifically proton-dominant events. Solar Proton Events are of particular concern for spacecraft and crew safety due to the penetrating power of high-energy protons, which can lead to substantial radiation exposure, electronic disruptions, and potential health risks during intense solar activity. The impact of SEPs on spacecraft and crew is highly dependent on particle energy levels and flux, with more energetic particles posing a higher risk to systems and health [28].

The intensity and potential damage caused by SEPs vary widely between events. Some SEPs can carry enough energy to significantly affect electronic system operation or penetrate typical spacecraft

shielding, requiring additional protective measures for electronic and human safety [19].

C.1.2. Galactic Cosmic Rays

Galactic Cosmic Rays (GCRs), unlike SEPs, are high-energy particles originating from outside the Solar System, likely from supernova explosions and other astrophysical events with extreme energy outputs [7, 44]. GCRs encompass all naturally occurring elements in the periodic table, from hydrogen to uranium, although most of the particles have atomic numbers less than or equal to iron (Z=26). This can be clearly seen in Figure C.1. Approximately 98% of GCRs are composed of protons and heavier ions, of which about 85% are protons, 14% helium nuclei, and the remaining 1% are heavier nuclei such as lithium, beryllium, and iron. The other 2% of GCRs are electrons and positrons [41, 12].

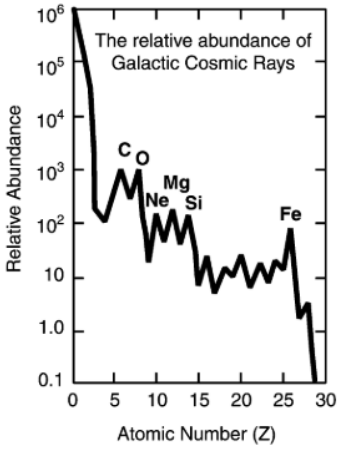

Figure C.1: Relative abundance of GCR up to Z=28 [7], data obtained from [41]

The energies of GCRs can reach as high as 10^{20} electron volts (eV), or 10^{11} GeV, making them extremely difficult to shield against, as even small fractions of these particles carry enough energy to penetrate significant shielding depths [39]. While GCRs have a continuous flux, their intensity fluctuates with solar activity; during solar minimum, GCR intensity increases due to the decreased influence of the heliospheric magnetic field, while it decreases during solar maximum [19].

GCRs pose a significant concern for space missions due to their high energies, stochastic nature, and potential for severe biological and electronic damage. Although less abundant than SEPs, GCRs carry heavy ions (like iron nuclei) that deliver a disproportionately high dose, as radiation dose increases with the square of the atomic charge, making them especially hazardous to biological tissue [39]. These isotropic particles can collide with shielding materials, generating secondary radiation, often in the form of penetrating neutrons. Such secondary particles complicate shielding design, sometimes increasing rather than mitigating radiation exposure. Consequently, GCRs contribute roughly 80% of the total radiation dose absorbed by space crew, presenting a continuous hazard for long-duration and deep-space missions [8].

C.1.3. Trapped Particles

Trapped particles are energetic particles confined by Earth's magnetic field, originating primarily from GCRs and SEPs [39]. These particles move along geomagnetic field lines, spiralling between magnetic poles that act as mirrors, limiting their ability to penetrate deeply into Earth's atmosphere and contributing to phenomena like the auroras [29].
Two torodial sahpes belts are present around the Earth and they are called the Van Allen belts, from the name of their discoverer.Section C.5. The trapped particles consist mainly of protons, reaching energies up to $600\,\mathrm{MeV}$, and electrons with energies as high as $10\,\mathrm{MeV}$, with other ions present in much smaller amounts [29]. The inner belt is primarily formed by protons and electrons resulting from the decay of neutrons created during interactions of cosmic particles with atmospheric atoms. The outer belt is filled mostly by solar particles injected during magnetic disturbances caused by particle

events hitting Earth [40].

The distribution of these particles varies across the Van Allen belts, with electron intensity peaking at altitudes of 0.5 and 4 Earth radii, while proton intensity is highest at about one Earth radius. Additionally, in the South Atlantic Anomaly (SAA), a region approximatemelylocated over Brazil, localised increases in radiation levels can be found[39]. The SAA results from the tilt of the magnetic axis (approximately 11°) and the offset of Earth's magnetic field axis by 450 km. This region dips as low as 200 km, contributing significantly to radiation exposure during spaceflight, particularly for low-inclination orbits passing through the SAA up to six or seven times daily [46].
The intensity and distribution of trapped particles are influenced by the solar cycle, with proton intensities rising with increased solar activity, while electron intensities decrease. This variation affects radiation exposure for satellites and space missions, especially in Low Earth Orbit (LEO), where particles in the SAA can deliver significant radiation doses in brief intervals during orbital passes [39].

C.2. Effects of Radiation on Spacecraft and Space Missions

C.2.1. Biological Effects of Radiation

Radiation in space poses risks due to the presence of high-energy particles, including Galactic Cosmic Rays (GCRs), Solar Energetic Particles (SEPs), and Trapped Particles which are not encountered on Earth. In LEO, astronauts and spacecraft are protected mostly by the Earth's magnetosphere. However, there are still varying degrees of radiation exposure, of which most is absorbed during the passage through the SAA where the magnetic field is less strong [30].

Acute Effects
Short-term or deterministic effects occur only above a threshold dose and are generally caused by high levels of exposure, such as those from intense SEPs. In cases of severe SEP exposure, acute effects can include Acute Radiation Syndrome (ARS), characterised by symptoms like nausea, vomiting, and immune system suppression. Other short-term effects may involve skin damage or temporary cognitive impairment due to central nervous system impacts during extravehicular activity (EVA) or high radiation dose events [19, 40].

Long-Term Effects
Due to the constant low flux of GCRs and sporadic SEPs, stochastic effects or probabilistic health impacts are of primary concern in long-duration missions. Research has shown that radiation exposure in space may increase risks of cancers, cardiovascular disease, central nervous system degeneration, and digestive issues. Additional potential impacts include immunological, endocrine, and genetic alterations [11, 49]. Another concern is the risk of neurodegenerative conditions such as Alzheimer's or Parkinson's disease, potentially made worse by GCR exposure over extended missions [19].

Cellular and Molecular Damage
At the cellular level, space radiation can cause direct DNA damage, including single- (SSB) and double-strand breaks (DSB), as well as indirect damage through the generation of reactive oxygen species (ROS), which can overwhelm cellular repair mechanisms [30]. High-LET radiation, such as heavy ions in GCRs, creates dense ionisation tracks that are especially damaging to DNA, often resulting in clustered DNA damage that is difficult for cells to repair, leading to mutations, chromosomal abnormalities, and potentially cell death [19].

Challenges of Heavy Ions and LET
Heavy ions, a component of GCRs, pose unique challenges due to their high LET, which intensifies their biological impact relative to low-LET radiation like gamma rays. The damage caused by these heavy ions is not mitigated by traditional shielding and is known to cause significant biological harm at low dose rates over time. The high-energy particles present in GCRs have biological effects that are disproportionate to their physical dose, leading to uncertainties in risk assessment, particularly at low dose rates found in space [49, 40].

Radiation Protection Measures
Given the varied biological impacts, radiation protection in space is guided by the ALARA (As Low As Reasonably Achievable) principle, aiming to minimise exposure through shielding and operational adjustments. However, shielding is largely ineffective against GCRs due to their high penetration capability, highlighting the need for advanced materials and strategies to mitigate these risks on long-duration missions [10, 42]. More about this in Section 2.3.

Overall, radiation exposure in space presents both immediate and delayed health risks for astronauts, with the potential to affect nearly every organ system. Understanding and mitigating these effects are absolutely necessary for future human space exploration, particularly beyond LEO, where exposure levels are higher.

C.2.2. Effects on Electronics

Following the biological effects of radiation in space, non-biological effects on spacecraft are also significant, particularly due to the damaging impact of high-energy particles on electronic and structural components. These effects can compromise mission longevity and reliability, and are generally categorised into Total Ionising Dose (TID), Displacement Damage (DD), Single Event Effects (SEEs), and Surface Charging (SC) [36, 50]. For this research, mainly these non-biological effects will be of interest as the flight data used in this work come from a communication satellite and no humans or biological tissue is present.

Total Ionising Dose (TID)
TID results from cumulative radiation exposure, specifically from ionising particles like protons and electrons. As these particles pass through materials, they deposit energy that can ionise atoms, creating charge accumulation. In electronics, this can lead to issues like increased leakage current and degraded component performance, especially in materials like silicon dioxide at critical interfaces. Over time, TID can cause malfunctions or even complete component failure, particularly in integrated circuits commonly used in satellites [24]. In LEO, TID exposure is influenced by trapped protons in the South Atlantic Anomaly and electron flux from the radiation belts, with doses varying based on orbit altitude, duration, and shielding [46].

Displacement Damage (DD)
Displacement damage occurs when high-energy particles (e.g., protons or neutrons) collide with atoms in a material, displacing them from their lattice positions and creating structural defects. This displacement can alter material properties, leading to reduced performance in semiconductor devices. Common effects of DD include increased leakage current in transistors and degradation of solar cells, which rely on a stable crystalline structure to function effectively. DD effects are cumulative, meaning that they worsen with prolonged exposure to the radiation environment in space [24, 36]. Factors influencing DD include particle type, energy, and material composition, with impacts varying across different electronic components [46].

Single Event Effects (SEEs)
SEEs are caused by individual high-energy particles (protons or heavier particles from GCRs)depositing enough energy in a device to induce immediate effects, either destructive or non-destructive. Over the years, many SEEs have been identified and have been classified into more precise groups. A few well-known classifications of SEEs are given below. The first is an example of a non-destructive SEE and the latter two of destructive ones [24, 46, 48].:

- Single Event Upset (SEU): a bit flip or memory error, often occurring in sensitive electronics.
- Single Event Latch-up (SEL): a more severe effect that can cause a device to lock in a high current state, potentially leading to permanent damage.
- Single Event Burnout (SEB) and Single Event Gate Rupture (SEGR): destructive effects that can irreparably damage power transistors and other sensitive circuits.

SEEs are particularly challenging to mitigate, as shielding in not very effective for the high-energy particles. Mitigation strategies typically focus on circuit design techniques, such as redundancy, error detection and correction codes and fault-tolerant components, to help manage and correct SEE-induced errors [24].

Spacecraft Charging (SC)
Spacecraft charging, both surface and internal, arises from interactions with high-energy particles and solar radiation, leading to electrostatic potential build-up. Surface charging, primarily due to low-energy plasma and photoelectric effects, can cause differential charging on spacecraft surfaces. Internal charging, from high-energy electrons penetrating deep into the spacecraft, poses a greater threat, potentially causing electrostatic discharges that can damage components. These discharges are a great hazard in spacecraft electronics, as they may lead to severe operational anomalies or degrade material properties over time [46].

C.3. Interaction of radiation with matter

C.3.1. Protons

In radiation, protons interact with matter in four primary ways: Inelastic Coulomb interactions with atomic electrons, Elastic Coulomb interactions with nuclei, Elastic or Inelastic collisions with nuclei, and bremsstrahlung.

Inelastic Coulomb Interactions with Atomic Electrons
As protons travel through matter, they gradually lose kinetic energy due to frequent inelastic Coulombic interactions with atomic electrons, a process sometimes termed ”stopping.” In these interactions, energy is transferred from the proton to an electron, which may be ejected from its atom [31]. Due to the substantial mass difference between protons and electrons, protons continue nearly along their initial trajectory despite this energy loss [34]. As the proton slows, the likelihood of additional interactions increases, resulting in a heightened energy loss rate near the end of its path, forming the characteristic Bragg peak [31].

Elastic Coulomb Interactions with Nuclei
Scattering occurs when a proton encounters the Coulomb field of a nucleus. Given the nucleus’s positive charge and significantly larger mass, protons are deflected from their original paths through elastic interactions which can be seen in Figure C.2b. Although each individual scattering event causes a minimal directional change, the cumulative effect of many such interactions leads to beam spreading, resulting in a Gaussian lateral profile. This scattering is more pronounced in high-Z materials, where the Coulomb interactions are stronger [31].

Elastic or Inelastic Collisions with Nuclei
Protons may occasionally engage in direct collisions with atomic nuclei. These nuclear interactions can be elastic, where the proton’s energy and trajectory remain mostly unchanged, or inelastic, wherein the proton enters the nucleus [31]. Inelastic nuclear reactions often produce a variety of particles, including secondary protons, neutrons, and light ions, which can interact further and generate a ”low dose halo” around the primary beam [34]. At higher energies, such interactions can initiate a cascade of secondary hadrons and gamma rays, further affecting the shielding requirements in space [27].

Bremsstrahlung
While typically less relevant in terrestrial radiotherapy [34], bremsstrahlung can be significant in the high-energy environment of space radiation. Here, high-energy protons can have electromagnetic interaction with a free electron causing the so-called inverse or proton-electron bremsstrahlung [20]. This process is quite similar to the more common electron bremsstrahlung, which will be discussed in Section C.3.2, except that the centre of momentum of the proton-electron system is practically the same as that of the energetic proton itself [18]. It causes the emission of $\gamma-$ and X-rays and was believed to contribute to the diffuse gamma-ray background and hard X-rays observed in solar flares [20].

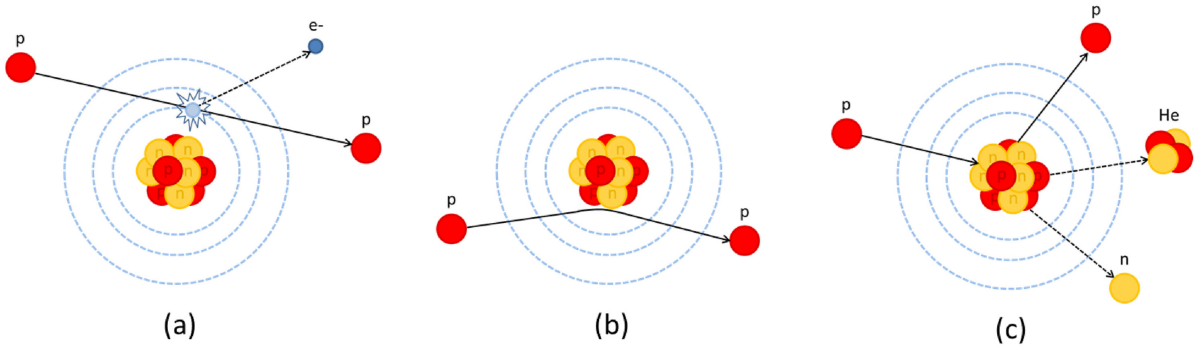

Figure C.2: Interaction of protons with matter. a) Inelastic Coulomb interactions with atomic electrons b) Elastic Coulomb interactions with nuclei c) Elastic or inelastic collisions with nuclei [31]

C.3.2. Electrons

When electrons interact with matter, they undergo several types of interactions that result in energy transfer and directional changes. These interactions are influenced by the electron's energy and the atomic properties of the target material.

Excitation

Excitation happens when an incident electron passes an atom at a sufficient distance to transfer energy, raising an atomic electron to a higher energy level without ejecting it, as seen in Figure C.3. The excited electron eventually returns to its ground state, releasing the excess energy as a photon. This process involves an energy transfer, often in the range of a few electron volts (eV) [31, 37].

Ionisation

Ionisation occurs when an incident electron passes close enough to an atom to transfer kinetic energy to an orbital electron, and ejecting it. This causes the atom to lose an electron and become an ion. The incident electron continues on a different path with reduced energy. Although ionisation events are less common than excitation events, they involve more significant energy transfer. This makes ionisation a key mechanism in energy deposition by electrons in matter [31, 37].

Bremsstrahlung

Bremsstrahlung, or "breaking radiation," occurs when an electron is travelling close enough to the nucleus of the atom that their Coulomb fields interact. This causes the incident electron to be deflected, resulting in deceleration and energy loss that is emitted as a photon. This process is more probable at higher electron energies and in materials with higher atomic numbers (proportional to Z^2) [31]. According to Katsumura et al., about 50% of the electrons undergo Bremsstrahlung when the electron beam has energies of 90 MeV [25]. At energies above a certain threshold known as the critical energy T_c, bremsstrahlung becomes the dominant mechanism of energy loss. An approximation is given by Berger et al. with the simple Equation C.1 where Z is the atomic number [6]. For Tungsten, this critical energy is approximately 10.6 MeV [37]. For Aluminium, this critical energy would be around 56 MeV. Looking at the radiation environment in LEO, the electrons reach energies up to 10 MeV as seen in Section C.1.3. The fraction of bremsstrahlung will therefore not be dominant but it is still advised to take it into account.

$$T_c = \frac{800}{Z + 1.2} \quad [MeV] \tag{C.1}$$

C.3.3. Gamma and X-rays

Gamma rays and X-rays, both high-energy electromagnetic waves, interact with matter in processes that reduce (or attenuate) their intensity as they pass through materials. This interaction is similar to the way ultraviolet rays and visible light are absorbed in matter, although gamma and X-ray interactions involve higher energy levels [25]. The interaction mechanisms for gamma rays and X-rays vary based on their energy and are primarily characterised by three phenomena: the photoelectric effect, the Compton effect, and pair production [45].

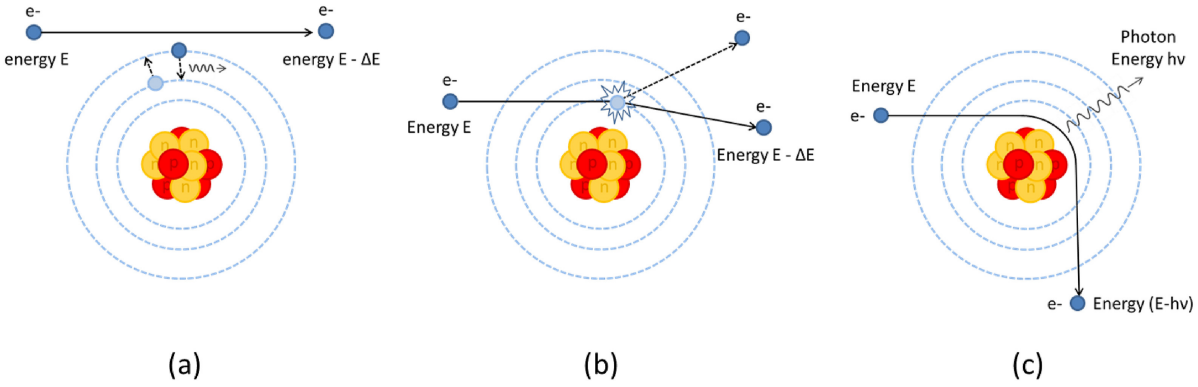

Figure C.3: Interaction of electrons with matter. a) Excitation b) Ionisation c) Bremmstrahlung [31]

Photoelectric Effect
At low photon (X-rays and γ-rays are photons) energies (less than hundreds of keV), the photoelectric effect is the primary mode of interaction. Here, photons transfer their energy to electrons in the material, causing these electrons to be ejected as photoelectrons. This process allows the material to absorb the photon's full energy, resulting in significant attenuation at lower energies [25].

Compton Effect
As the photon energy increases (into the hundreds of keV to several MeV), the Compton effect becomes dominant. In this interaction, the incoming photons collide with electrons, transferring part of their energy to the electron, which is then emitted with increased energy. The photon, now with reduced energy, is scattered in a different direction, leading to partial energy absorption by the material [25].

Pair Production
For very high photon energies (above 1.022 MeV), pair production becomes the primary interaction mechanism. In this process, the photon's energy is converted into a positron-electron pair, facilitated by the nearby atomic nucleus. The positron and electron are emitted in opposite directions, with the amount of kinetic energy depending on the photon's original energy [9].

When gamma rays enter a medium, they interact through above mentioned methods, depending on the gamma ray's energy as seen in Figure C.4. These interactions produce secondary electrons, which then interact further with matter, leading to physical, chemical, and biological effects. Given this chain of interactions, gamma-ray irradiation can, as a rough approximation, be considered equivalent to electron beam irradiation, producing similar effects [25].

C.4. Solar Activity

The Sun undergoes an approximately 11-year cycle of activity, characterised by alternating periods of high and low solar activity. During solar maximum, solar magnetic activity intensifies, resulting in an increased frequency of solar flares, coronal mass ejections (CMEs), and a strengthened solar wind [17]. This enhanced solar wind can deflect GCRs with energies below 1 GeV/nucleon, reducing their flux near Earth, while simultaneously amplifying the energy of SEPs. Conversely, during solar minimum, the weaker solar wind allows a greater influx of GCRs into the solar system. Although the solar wind itself poses minimal threat due to its low-energy particles, it plays a critical role in modulating space radiation, impacting both GCR and SEP dynamics in Earth's vicinity [39].

C.5. Earth Magnetic Field

Earth's magnetic field, primarily generated by a dynamo effect in its iron core, creates a magnetic dipole structure tilted about 11° from the planet's rotational axis, forming the magnetosphere [44]. This magnetosphere traps high-energy particles within the Van Allen Belts, which consist of an inner and an outer belt. The inner Van Allen Belt, extending from about 1,000 to 13,000 km above Earth, primarily contains energetic protons with energies above 30 MeV and some high-energy electrons. In contrast,

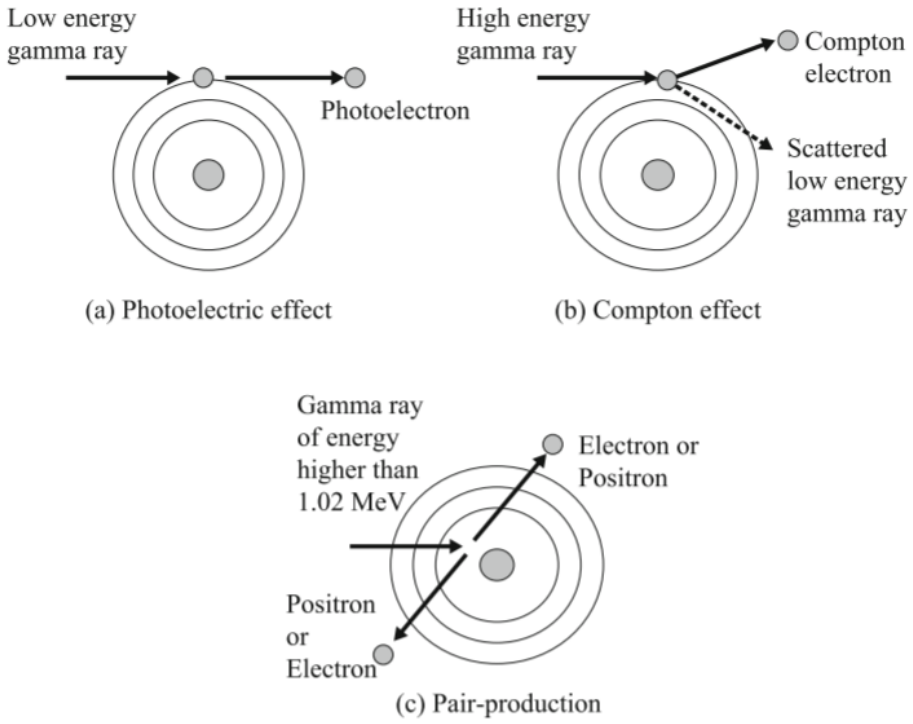

Figure C.4: Interaction between photon (γ- or X-ray) and material [25]

the outer belt, ranging from around 19,000 to 40,000 km, is dominated by relativistic electrons and lower-energy protons [44, 21].

Trapped particles in the magnetosphere follow three characteristic motions: gyrating around magnetic field lines due to the Lorentz force (see Equation C.2), bouncing between magnetic poles, and the east-west drift where positive charges drift westward, and negative charges drift eastward [29]. These movements are constrained by the magnetic field, with particles reflecting at ”mirror points” near the poles. In certain areas, such as the South Atlantic Anomaly (SAA), the inner Van Allen Belt is closer to Earth’s surface due to distortions in the magnetic field, resulting in higher radiation exposure for low-altitude orbits in this region [44].
Below, the equation of the Lorentz force is given:

$$\mathbf{F} = q(\mathbf{E} + \mathbf{v} \times \mathbf{B}) \tag{C.2}$$

With F being the force, q the charge of the particle undergoing the force with a velocity v. E is the electric field and B the magnetic field. When looking at this equation, it becomes obvious that when particles come in at a $90°$ angle, they will experience the highest force and will have the largest redirection (due to the cross-product) while particles following the field lines will not be redirected at all.

The magnetosphere shields against lower-energy particles, but high-energy GCRs and SEPs can penetrate during geomagnetic storms. This shielding effect varies by latitude and altitude, with increased particle exposure at high inclinations and in regions with lower cut-off energies, such as the poles and the SAA [44]. Each point in the magnetosphere has a geomagnetic rigidity cut-off proportional to the perpendicular magnetic field component. For particles to reach a specific point, their rigidity (momentum divided by charge) must exceed this cut-off. The rigidity is a function of latitude, increasing from the poles (where the cut-off is zero, allowing entry of particles with any energy) to the equator [40].

C.6. Limitations of Current Radiation Models and Measurements

The AP-8 and AE-8 models are the most commonly used descriptions of the trapped proton and electron environment around Earth. Despite their widespread use, these models have well-known limitations. They are static models, providing only average fluxes for solar maximum or minimum conditions, without accounting for the strong spatial and temporal variations in the radiation belts [23]. Data from the CRRES mission revealed that these variations are far more dynamic and complex than AP-8 and AE-8 can capture [16, 22].

Additionally, these models are based on data from the 1960s and 1970s and exclude high-energy solar events, making them less reliable during periods of increased solar activity [16]. Large discrepancies have been observed between predicted and measured radiation doses, sometimes differing by a factor of two or more, depending on shielding and orbit conditions [16].

While more advanced models like AE-9/AP-9 exist and offer statistical uncertainty estimates based on broader datasets [2], this study attempted to use AP-8, AE-8, and CRRES models for consistency and practical reasons. Importantly, these models describe the unshielded environment, whereas onboard measurements, such as those from the TPX3 detector on JoeySat, are taken behind shielding. This research therefore aims to bridge this gap by exploring whether data collected after shielding can be used to infer the external radiation environment. Due to the scope of this project, a detailed integration of these models was not performed and is therefore recommended for future work.